



VRIJE
UNIVERSITEIT
BRUSSEL



Thesis submitted in order to obtain the degree of Master of Science in Physics and Astronomy

BACKGROUND ESTIMATION FOR THE SEARCH FOR NEW PHYSICS IN DISPLACED DIMUON EVENTS WITH THE CMS DETECTOR AT CERN

**Search for supersymmetry particles with displaced
muon signature**

KAMAL A. SAOCHA
2017 - 2018

Promotor: Prof. Dr. Freya Blekman
Sciences and Bio-Engineering Sciences

Contents

1	Introduction and motivation	3
2	Theoretical overview	5
2.1	The Standard Model of fundamental particles	5
2.1.1	Fermions	6
2.1.2	Bosons	7
2.2	Extension necessity of the Standard Model	8
2.3	Supersymmetry as candidate for the SM extension	8
2.3.1	The Minimal Supersymmetric Standard Model (MSSM)	8
3	The Compact Muon Solenoid Experiment (CMS)	10
4	Data and Monte Carlo simulation	11
4.1	The CMS 2016 data	11
4.2	Monte Carlo simulation samples	12
4.2.1	Non-QCD background	14
4.2.2	QCD background	14
5	Events requirements and data selection	15
6	Control and Signal regions	16
6.1	Motivation	16
6.2	The Prompt Control region	16
6.3	The Displaced Control region	18
6.4	The Signal Regions	18
6.5	The $b\bar{b}$ control region	18
6.6	The $\mu\mu$ non-isolated control region	19
7	Non-QCD background estimation	19
7.1	MC and data agreement in the Prompt Control Region	19
8	QCD background estimation	23
8.1	Data-driven method	23
8.2	Closure test for the data-driven method	26
8.3	QCD estimation in the Signal Regions	32
9	Background estimation results	33
9.1	QCD background	33
9.2	Non-QCD Background	35

<i>CONTENTS</i>	2
10 Supersymmetric Top Quark Monte Carlo Estimation	35
11 Limits on the SUSY model	42
11.1 Systematic uncertainties on the background estimation	42
11.2 Limit setting	43
12 Comparison to Official CMS Results	51
13 Conclusion	54
13.1 Non-QCD background estimation	54
13.2 QCD background estimation	54
13.3 Results	54
13.4 Limits	55
14 Outlook	56
15 Summary	56
Bibliography	57

1 Introduction and motivation

Nowadays, Physics is on a whole other level, necessitating more complicated theories and experimental instruments. After successful predictions, such as the Brout-Englert-Higgs boson and the direct observation of gravitational waves, fundamental questions about our surroundings are still arising, often leading to searches for new physics theories. In fundamental particle physics, a large community of physicists are investigating in searches for physics beyond the so called Standard Model, a theory describing successfully the building blocks we know today, and their interactions (gravity excluded). Clearly, the Standard Model cannot be a theory of everything but is probably not incorrect, since its predictions were accurately observed many times.

Today, theoretical physicists have come with a large amount of potential theories for the extension of the Standard Model, sometimes predicting new undiscovered particles. One of these is the so called Supersymmetry, an elegant theory that can solve many open questions, such as the Dark Matter puzzle. On the other hand, experimentalists are digging in the available data, trying to test the predicted theories. This is typically done by looking for excesses over known physics backgrounds. Most of the time, the assumption is such that the new wanted particle is not directly detectable by the detectors, which is typically identified from its decay products or missing tracks in the reconstruction. The last decades, an important number of searches has been performed for model predicting prompt decays, i.e. particles with a negligible lifetime, and unfortunately there is still no indication for physics beyond the Standard Model. This led that some searches today to move in the direction of models predicting exotic particles that have a significant lifetime, enabling decays further away from the production vertex. These processes predicting displaced decays became a hot topic and are extensively tested in High Energy Experimental Physics.

In this thesis, a search for displaced decays is performed, looking for a Beyond the Standard Model process emerging from proton-proton collisions at 13 TeV center-of-mass energy. Although the search is based on a Supersymmetry model, the goal is to be sensitive to any model predicting the same signal signature. In the next chapter, a theoretical overview is given, starting with the Standard Model and its shortages, followed by a brief introduction to the Supersymmetry theory with the focus on the topology used in this search. Chapter 3 describes the experimental facility used to obtain data used for the analysis, which is the Compact Muon Solenoid detector located at CERN in Switzerland - France. In Chapter 4, the data and simulation

samples are shortly discussed. In Chapter 5, to filter interesting events in the data consistent with the assumed topology, a set of requirements and selection will be applied on the data-sets. The strategy for the Standard Model background estimation and the definition of the regions of interest that will lead to proper estimation of the signal are discussed in Chapter 6. The Standard Model background is further divided in QCD- and non-QCD background, because of the difference in the estimation method. In Chapter 7 and 8, we discuss the estimation methods of respectively non-QCD and QCD background. In Chapter 9, the results of the background estimation are presented for QCD and non-QCD. After the background contribution estimation in the region of interest, the signal yield of the assumed topology is simulated, presented in Chapter 10. Having these results, one can set limits on the cross section production of the assumed topology at the current center-of-mass energy. These are presented in Chapter 11, followed by a comparison to Official CMS results in Chapter 12. Although the results in this thesis show better results than the current official ones, it is believed that the analysis sensitivity can still be improved, showing higher limits when combining all the results. Therefore the data in the interesting regions will not be unblinded, so no conclusion is presented whether a signal has been found or not.

2 Theoretical overview

Since the dawn of time, physicists are aiming for one goal: the climax of the theory of everything, a theory for which no secret or paradox can exist. This hunt for the truth is far from being easy, and every time a discovery is made, new mysteries and questions arise, necessitating more sophisticated explanations and technology. This is currently the case in Particle Physics, where the smallest constituents of the direct and indirect observable universe are studied. A remarkable collaboration, from physicists around the world, led to the accomplishment of the Standard Model theory, describing particles interacting through three fundamental forces.

2.1 The Standard Model of fundamental particles

The Standard Model (SM) of fundamental particles is clearly a master piece in the history of science. It includes the work of 13 Nobelists since the 20th century and delivered accurate evidence of its predictions with no doubt. The SM is the theory for electroweak and strong interactions. Its rigorous mathematical description is formulated in Quantum Field Theory[1], starting from the idea of describing elementary particles as field quanta. These fields can interact with each other and their dynamical properties are summarized in the following Lagrangians [1]:

$$\mathcal{L}_{EW} = i\bar{\psi}\gamma^\mu\partial_\mu\psi - m\bar{\psi}\psi + g'\bar{\psi}\gamma^\mu\frac{\sigma_\alpha}{2}W_\mu^\alpha\psi + g\bar{\psi}\gamma^\mu\frac{Y}{2}B_\mu\psi, \quad (1)$$

$$\mathcal{L}_{QCD} = i\bar{\psi}\gamma^\mu\partial_\mu\psi - m\bar{\psi}\psi + g_s\bar{\psi}\gamma^\mu\frac{\lambda_\alpha}{2}\cdot G_\mu^\alpha\psi, \quad (2)$$

where the first one is the Lagrangian for the electroweak interaction and the second one for the strong interaction. The first two terms in both Lagrangians are known as the Dirac Lagrangian, describing half-spin particles, known as fermions, in an interaction-free relativistic regime. Here are ψ and $\bar{\psi}$ the Dirac spinors of the fermions, m their mass and γ^μ the Dirac matrices. Finding a set of symmetries of the system that leaves the Lagrangian invariant [1], leads to the additional terms describing the fundamental interactions between the fields. Here are the g 's the couplings, σ_α the Pauli matrices, λ_α the Gell-Mann matrices, and W_μ^α , B_μ and G_μ^α the gauge fields arisen from the symmetries [1]. From these gauge field, one can construct the physical boson fields,

$$W_\mu^\pm = \frac{1}{\sqrt{2}}(W_\mu^1 \mp iW_\mu^2), \quad (3)$$

$$Z_\mu = W_\mu^3 \cos\theta_W - B_\mu \sin\theta_W, \quad (4)$$

$$A_\mu = W_\mu^3 \sin\theta_W + B_\mu \cos\theta_W, \quad (5)$$

where the first two fields corresponding to the weak force carrying bosons, respectively the electric charged W -bosons and the electric neutral Z -boson. The last one is the photon field, which is the massless electric neutral boson responsible for electromagnetic interactions. From Equation 2, the fields G_μ^α of the strong force carrying bosons, called the gluons, are directly given.

Summarizing the content of the SM theory, the elementary particles are classified through their spin-number, resulting in two groups, the fermions and the bosons.

2.1.1 Fermions

The fermions are further separated in quarks and leptons. Quarks have a fractional electric charge and are sensitive to strong interactions, while leptons have integer electric charge and do not interact strongly. Because quarks can interact with strong forces, an additional kind of charge is attributed, called the color charge, which is described in Quantum Chromodynamics (QCD) [1], an analogical theory to Quantum Electrodynamics for electromagnetic interactions. Moreover, fermions appear to exist in three generations, where the properties are indifferent in each generation, except for their mass. In Table 1, the three generations of the distinct quarks and leptons are shown.

Table 1: The fermions categorized depending on their proprieties

	Fermions			Strong	EM	Weak	Electric charge
Quarks	u	c	t	x	x	x	+2/3
	d	s	b	x	x	x	-1/3
Leptons	e	μ	τ		x	x	-1
	ν_e	ν_μ	ν_τ			x	0

On top of this, the SM predicts also the existence of particles having the same properties as the generic fermions, but with an opposite charge. This was first realized by Paul Dirac, when he wrote the Schrödinger wave function for the electron, taking in account Special Relativity. Doing the bookkeeping, there are 6 flavors and 3 colors for quarks, which gives 18 quarks. Adding

6 leptons results in a total of 24 generic fermions. Doubling this number because of the corresponding anti-particle of each fermions, a total of 48 fermions is obtained in the SM. For so far we know, the matter we can see today is only made of bound states of first generation quarks, called protons and neutrons, which are surrounded by electrons, forming atoms.

2.1.2 Bosons

As mentioned before, QFT is the theory describing the fundamental forces, except gravitation. It does it by introducing gauge bosons, which act as force carriers, exchanged during an interaction. Like photons carry electromagnetic force, the gluons are the strong force carrying particles, while the Z - and the W-bosons are those for weak interaction. The SM interactions are described by three-point vertices, where the gauge bosons are coupled to fermions. A particle can interact through a force, only if it carries the corresponding charge. Similar to the electric charge in electromagnetism, the strong and weak force also have a characteristic charge, which is respectively the color charge and the isospin. All fermions carry isospin and consequently they all interact weakly, but only quarks do carry color charge and thus they can interact strongly. Finally these fundamental forces can be compared in function of their strength. In Table 2, the relative strength of each interaction (including gravity) is shown for a two-body system separated by roughly the proton radius. It is important to know that this comparison is not energy independent [1].

Table 2: The relative strengths of the four fundamental forces

Force	Strength	Boson	Mass
Strong	1	Gluon	0
Electromagnetism	10^{-3}	Photon	0
Weak	10^{-8}	W^\pm, Z	80.4, 91.2 GeV
Gravitation	10^{-37}	?Graviton?	0

Finally, there is one last boson that was the cherry on the cake for the SM predictions, called the Brout-Englert-Higgs boson. It is described in QFT as a field being extended over space-time, with a non-zero expectation value everywhere, even in vacuum. A particle interacting with this field acquires mass. The boson has been detected in 2012 by two detectors at CERN (CMS and ATLAS experiment), having a mass of 124 ± 0.28 GeV [2]. Unlike other bosons, the Higgs boson is scalar spin-less particle.

2.2 Extension necessity of the Standard Model

Although there is no doubt about the precision of the SM, it is certainly not complete, in the sense that there are still questions that the SM does not solve. It is very likely that the SM needs only an extension rather than being reformulated, due to its success and its precision. A few other examples of the shortcomings of the SM than gravity are the identification of Dark Matter [3], the Hierarchy problem between the fundamental forces, and the large number of arbitrary parameters. Theorists have already prepared a few potential theories to explain some of the encountered shortcomings. The most famous extensions are Supersymmetry, the large-scale extra dimensions and the promising but very difficult demonstrable String theory. From now, the focus will further lie on Supersymmetry, since the search considered in this thesis is based on it.

2.3 Supersymmetry as candidate for the SM extension

Supersymmetry, also referred to as SUSY, is one possible missing puzzle explanation to solve the limitations of the SM. It solves enigmas by adding elementary particles, which can be candidates to solve problems, such as Dark Matter, or the renormalization of the Higgs mass [3]. The main idea behind SUSY, is to add for each SM particle a corresponding supersymmetric particle, also referred to as a sparticle, having a spin with a difference of $1/2$. Thus SM fermions would have spin-less scalar super-partners, being bosons, and SM bosons would have half-integer spin super-partners, being fermions. From this symmetry, one would have discovered these sparticles if Supersymmetry was an exact symmetry [3]. But the fact that it is not already observed, it would suggest that SUSY is broken, assuming the theory is true. If this is the case, the Lagrangian introduced by Supersymmetry must be composed of a term preserving symmetry and a second one for the symmetry-breaking,

$$\mathcal{L}_{total} = \mathcal{L}_{SUSY} + \mathcal{L}_{break}. \quad (6)$$

This symmetry-breaking term needs to be chosen very carefully to obtain the desired properties[3], and also often referred to as the soft-supersymmetry-breaking term.

2.3.1 The Minimal Supersymmetric Standard Model (MSSM)

In general, Supersymmetry is included in several scenarios, which gives various different models within the theory [3]. Typically the choice and the number of free parameters in these models is different. Models with the least

number of free parameters are categorized under Minimal Supersymmetric Standard Model (MSSM). In this class of models, a sparticle is attributed to each fermions and bosons, making the assumptions that there is a Grand Unification of the three fundamental forces in the SM at high energies, and that the mass of the superpartners of fermions are equal at the Grand Unification scale. Also, a new conserved quantum number is introduced, called the R-parity, which is given by,

$$R = (-1)^{2S+3B+L}, \quad (7)$$

where S is the spin, B the baryon number and L the lepton number. The value of R equals unity for all SM particles, and -1 for all their superpartners. A consequence of this conservation is that sparticles must be created in pairs. This results in the stability of the lightest sparticle, being a good candidate for Dark Matter [3]. It also reduces the number of free parameters considerably [3].

However, there are also models predicting processes where the R-parity conservation is violated [4]. From equation 7, this would imply that the Baryon or the Lepton number is violated. This is a delicate matter for the Baryon number, since it interferes with the fact that the proton is stable, and its decay has not been observed yet. So it is more likely considered that the lepton number is violated.

In this thesis, a topology of a R-parity violating model is assumed as an example. It predicts the production of the supersymmetric top-quarks, called the stop. The stop quarks are produced in pairs and are considered to have a significant lifetime in order to decay further away from the primary vertex. The R-parity violation is manifested in the decay, where each stop decays in a lepton and a bottom-quark. In each vertex, $R_{before} = R_{stop} = -1$ and $R_{after} = R_{lepton} * R_{b-quark} = 1$, and thus not conserved. These stops are considered to be each others antiparticle, so the leptons and the b-quarks must have an opposite charge. In this search, only the leptons are considered in order to make the analysis as model-independent as possible. In principle, there are multiple scenarios in this leptonic final state. The work presented here includes the opposite charged $\mu\mu$ final state. In Figure 1, a schematic representation of the stop quark production scenario is illustrated.

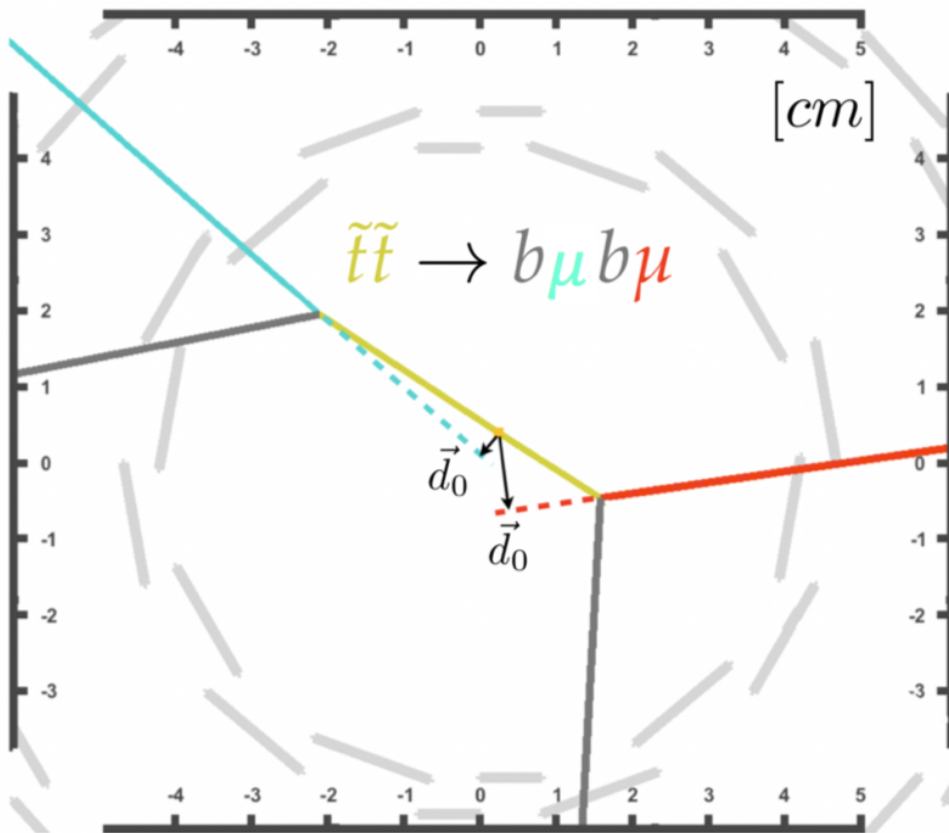


Figure 1: Schematic representation of the stop quark pair production scenario decaying in two displaced muons and b-quarks [4]

3 The Compact Muon Solenoid Experiment (CMS)

In order to enable experimental observations of predictions in QFT, huge facilities and experiments are unavoidable. One of the world's biggest research organization in (among other fields) Particle Physics is based at the European Organization for Nuclear Research (CERN), situated around the borders between Switzerland and France. It is famous for its world's largest particle accelerator, the so called Large Hadron Collider (LHC), colliding protons, currently at 13 TeV center-of-mass energy. This chef-d'oeuvre has been sculpted by scientists and engineers from around the globe. The LHC is planted 175 meters under the Swiss-French territory and has a circumference of 27 km. There are four interaction points, where the proton-proton collision events are recorded by four immense detectors.

One of these detectors is the cylindrical shaped Compact Muon Solenoid Experiment (CMS). It is composed of a massive solenoid magnet several layers of detectors, built around the interaction point. The first layer represents the tracker, crucial in the determination of the particles momentum, made of pixels and silicon microstrips. The second layer consist of a the electromagnetic calorimeter, which is important in energy measurements of electrons and photons. The third layer includes the hadronic calorimeter used for measuring the energy of hadrons. In the fourth layer, the gigantic superconductive magnet generates a 4 Tesla magnetic field, curving charged particles depending on their momentum, allowing in the determination of their mass/charge ratio. Finally the fifth layer, which represents a prominent task of CMS, are the muon chambers, designed to detect muons, since they can travel through the previous layers without being stopped.

The CMS experiment is known for a wide physics program. Currently, searches for Beyond the Standard Model physics are about 50 % of the hundreds of results published by the CMS community, where among them searches similar to the one considered in this thesis.

4 Data and Monte Carlo simulation

In most High Energy Experimental Particle Physics searches, the procedure for testing models consists of simulating the understanding of the underlying physics, based on the assumed theory. Having the characteristics of the experimental facility, in this case the CMS detector, one can simulate the various subatomic processes occurring in proton-proton collision events. Given the cross section of the known processes, it is also possible to estimate the number of events in the available data, taken during a certain operating period, called a Run.

4.1 The CMS 2016 data

As mentioned before, the data used in this thesis were taken in 2016 by the CMS detector. During this year, the data collected were divided in different Runs. For each Run, one can associate an integrated luminosity, \mathcal{L} , which reflects the size of the data collection, i.e. the number of events per unit area collected during the Run. In Figure 3, the recorded total integrated luminosity in 2016 is plotted during the operating period. Note that the curve is cumulative, and thus not decreasing. The periods during which the

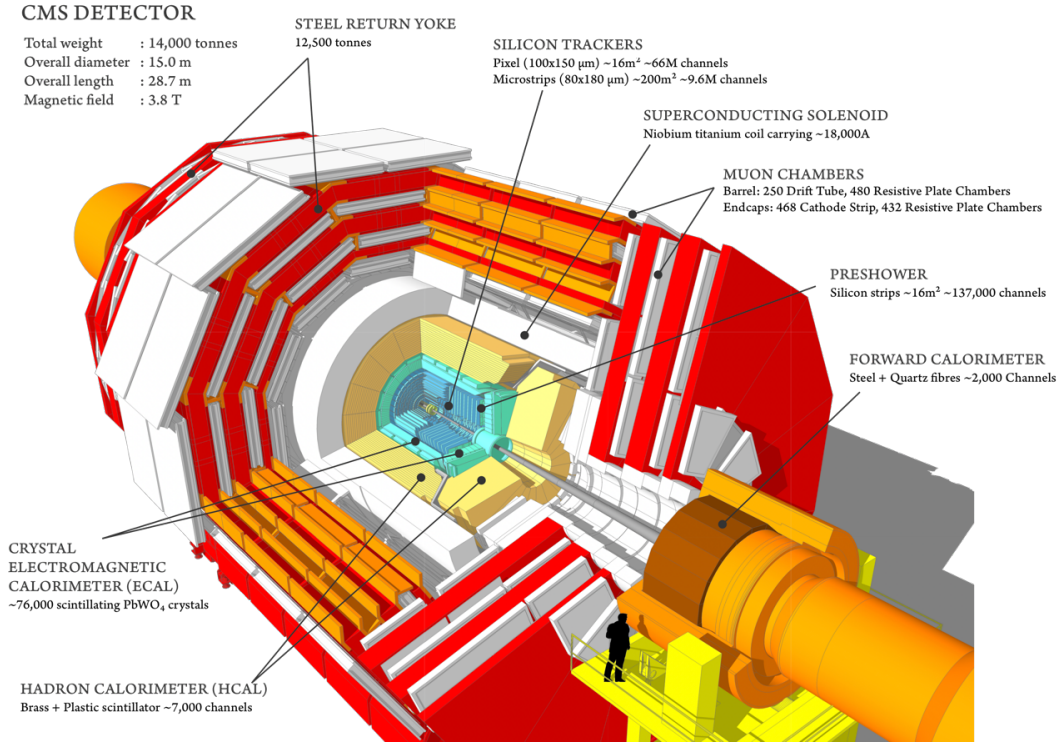


Figure 2: Representation of the Compact Muon Solenoid detector and its different layers and components based at CERN. [5]

integrated luminosity is constant represents time-intervals when no data were recorded. Counting the data of all Runs (referred as Run B, C, D, E, F, G, H), a total of $\mathcal{L} = 35.76 \text{ fb}^{-1}$ was recorded at 13 TeV center-of-mass energy.

4.2 Monte Carlo simulation samples

In order to understand the physics behind the number of events in the data, it is necessary to simulate the theory and try to obtain a data-simulation agreement. For instance, indications of new physics can occur in excesses over the simulated data from well-known physics, suggesting that there are other processes that should be taken in account in order to understand the full data-set.

It is important to figure out the contribution of the background, which are by definition SM processes giving the same final state as the assumed topology signature. To obtain the expected number of events, N_i , of a certain

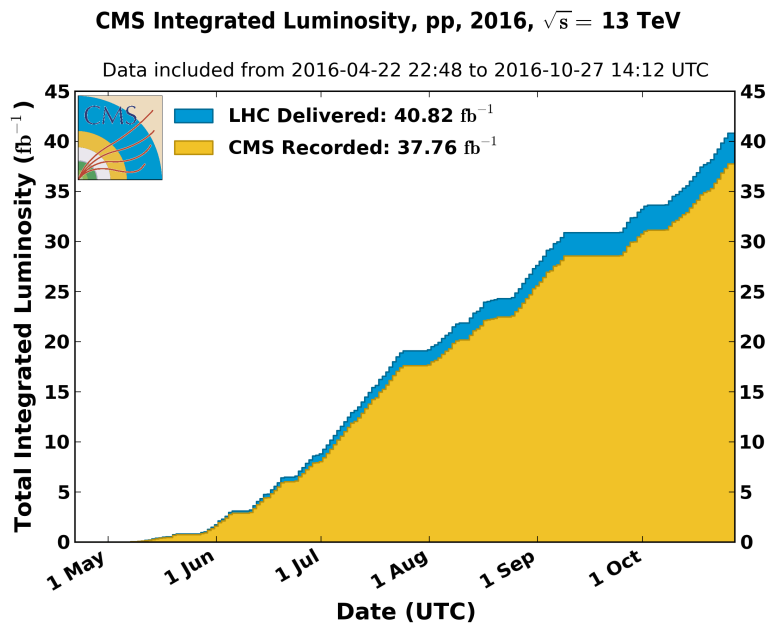


Figure 3: Cumulative integrated luminosity for the data taken in 2016 with the CMS detector [4]

subatomic process,

$$p + p \rightarrow (X + \dots \rightarrow) \dots + \mu\mu, \quad (8)$$

with a cross section σ_i , given \mathcal{L}_j the integrated luminosity of the corresponding j -th Run, one can use the following relation,

$$N_i = \mathcal{L}_j * \sigma_i, \quad (9)$$

where i denotes the i -th process. However the number of simulated events is not equal to N_i , so it must be scaled w.r.t. \mathcal{L}_j using a normalization factor n_f ,

$$n_f = \frac{\mathcal{L}_j * \sigma_i}{\tilde{N}_i}, \quad (10)$$

where \tilde{N}_i represents the number of simulated events, which is multiplied by the n_f to recover N_i .

Before considering the processes that has a significant cross section to contribute as background noise to the signal, we divide the background in two groups following their method of estimation; the QCD- and Non-QCD background.

4.2.1 Non-QCD background

There are five important sources in the SM that can produce events with two muons in the final state. These processes occur in proton-proton inelastic collisions. First, the Drell-Yan process, where a quark and its anti-particle annihilates to create a photon or Z-boson that can decay to two opposite charged muons. The production of two electroweak bosons decaying in muons and neutrinos. Top and anti-top quark production resulting in muons, quarks and neutrinos final state. A single top quark produced with a boson, which results in at least two muons. Finally, production of a W-boson with a jet can lead to two muons and quarks in the final state.

For all these non-QCD processes, a corresponding Monte Carlo (MC) simulation is performed for proton-proton collisions at 13 TeV, giving the expected number of events in function of parameters of interest, such as the momentum or the impact parameter of the produced muons. Using the normalization factor of the corresponding integrated luminosity, one can model the data with MC samples. In this search, the following MC generators are exploited; *PYTHIA*[7], *MADGRAPH* [8], *POWHEG* [9], *MC@NLO* [10] and *TAUOLA* [11]. One needs these different generators in order to produce the MC samples, which are very time consuming; it takes on average 2 minutes for produce one event (Drell-Yan \approx 40 million events).

4.2.2 QCD background

Quarks are quite complex to identify and necessitates a different approach. In fact, they were never directly observed, such as electrons or photons. This is a consequence of the Principle of Confinement [1], which does not allow the stability of free individual quarks. As soon as a quark is produced, the hadronization process happens quasi simultaneously. This results in a shower of colorless hadrons, called jets, which are reconstructed to enable the identification of the quark. However, simulating a reasonable size of samples with events giving two muons in the final state is computationally difficult. Therefore, QCD background will be determined from a dedicated method, discussed in Section 5, using the excess over non-QCD MC in control regions, where no signal is expected,

$$N_i(QCD) = N_i(data) - N_i(nonQCD), \quad (11)$$

where N_i is the number of events in the i-th bin of the considered histogram, including data and MC.

5 Events requirements and data selection

Not all events including two muons are relevant for the analysis. Before starting looking to the data, one needs to restrict the samples by imposing requirements reflecting the properties wanted for the signal. This is done by the application of cuts on the muon collection, discriminated depending on the value of their parameters.

The event selection starts with the requirement that only events with two muons are selected. For reconstruction efficiency reasons [6], muons with a pseudo rapidity η higher than 2.4 are rejected. The η is given by,

$$\eta = -\ln\left(\tan\frac{\theta}{2}\right), \quad (12)$$

where θ is the angle separation between the particle and the proton-beam. At $\eta = 0$ the particle is in the transverse plane, while at $\eta = \infty$ parallel to the beam direction. For this analysis, a dedicated trigger has been designed to select displaced muons. The efficiency threshold of this trigger is transverse momentum p_T dependent, therefore only events with muons having a p_T above the threshold ($p_T > 40$ GeV) are kept. Further, the muons are assumed to be isolated. The isolation requirement is translated as $I_{so} < 0.15$ defined as,

$$I_{so} = \frac{p_T^{surrounding}}{p_T^{muon}} \quad (13)$$

where the nominator represents the transverse momentum of particles within $\Delta R < 0.4$, the three dimensional angular separation around the muon, defining a cone given by,

$$\Delta R = \sqrt{\eta^2 + \phi^2} \quad (14)$$

with ϕ the azimuthal angle of the cone. Also the two muons are required to be separated with $\Delta R > 0.5$. Because the pair of supersymmetric particles are expected to be created, in a particle and antiparticle, muons from one event are required to have an opposite charge. Finally, misidentified reconstructed muons are also filtered using a method based on reconstruction requirements[6]. A summary of the stated conditions for an event to be selected are listed in Table 3.

Cuts and requirements for event selection
Two muons per event
Muons with $\eta < 2.4$
Muons with $p_T > 40$ GeV
Muons charge product $q_{\mu 1} * q_{\mu 2} = -1$
Muon isolation $Iso < 0.15$
Muons angular separation $\Delta R > 0.5$
Muons identified as real muons

Table 3: Cuts and requirements applied on the data and MC samples for the event selection

6 Control and Signal regions

6.1 Motivation

Having specified the events of interest assuming the Displaced SUSY topology and the final state, one need to define the "window(s)" where to look, where the signal is expected or at least enhanced with respect to the expected background. As mentioned before, the search is focusing on displaced muons, therefore the transverse impact parameter d_0 can be useful to consider, indicating how far the displaced vertex is removed from the interaction point. d_0 is defined as the closest separation of the linear-extrapolated muon path, in the plane perpendicular to the beam direction. The scheme in Figure 1 illustrate the latter definition.

There are two kind of regions needed for the strategy, in order to start the number of events estimation; the control and signal regions. The control regions are by definition regions where the data is claimed to be understood, and are used to model the non-QCD background with the data and also for the data-driven method to estimate the QCD. The signal regions are regions where the signal is expected to be larger than the background. The major task is to estimate the number of background events in these regions, in order to look for any excess in the data.

6.2 The Prompt Control region

The Prompt Control region (PCR) is defined in the two-dimensional d_0 -plane stretched by the transverse impact parameter of the two muons. It is the restricted area with only muons having a $d_0 < 0.01$ cm (Red-colored square Figure 4). This region is dominated by prompt processes, such as the Drell-

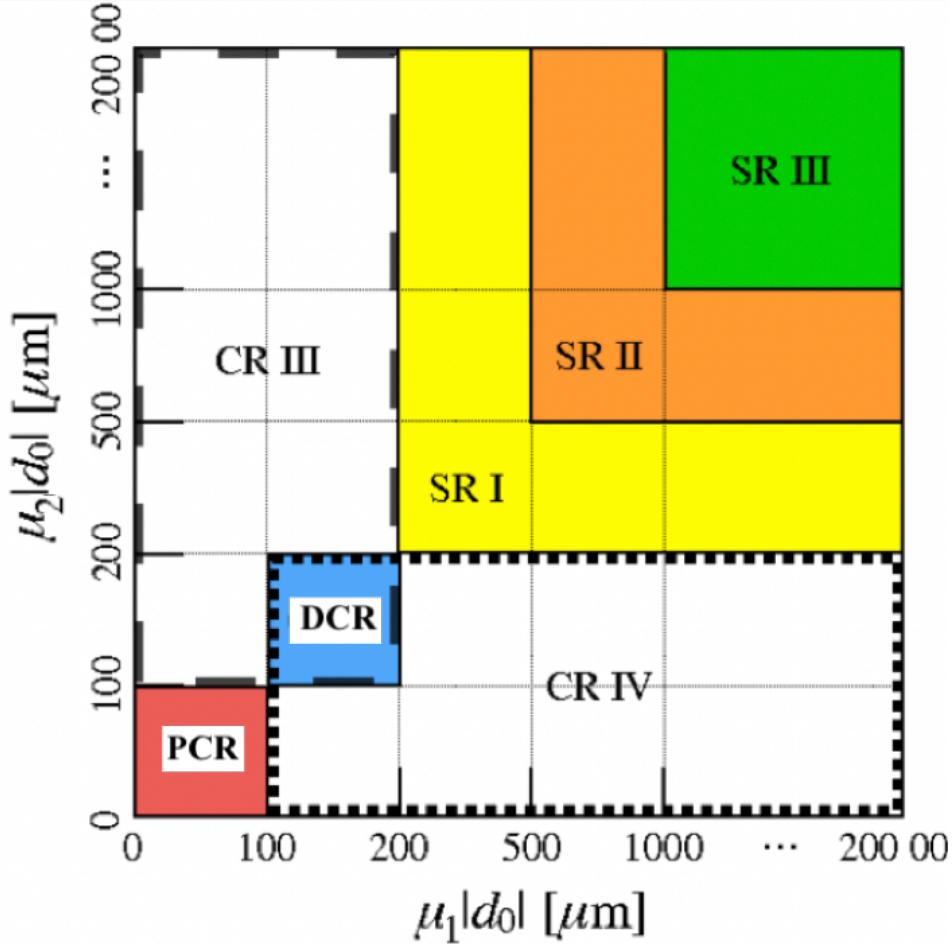


Figure 4: Definition of the Control and Signal regions in the 2D d_0 spectrum[6]

Yan process, which represents the most significant background source in that part of the spectrum. The PCR has a major importance in the MC-data agreement, which is used to obtain a reliable prediction that can be used to predict the background in the other regions. A first attempt is to normalize it with the corresponding normalization factor discussed in Chapter 4 (eq. 10). This appears to be not sufficient, other effects and corrections needs to be taken in account. In high-luminosity colliders such as the LHC, one single bunch crossing can produce various separate events, referred as pileup events. This is corrected on MC level, together with differences in the modeling of the identification and isolation efficiency of the muon, depending on their η and p_T . Once agreement is achieved in this region, one can trust the MC in order to predict number of events in regions of interest.

6.3 The Displaced Control region

The Displaced Control region (DCR) is the neighbor region of the PCR, and it is comprised of the area with only muons having a d_0 between 0.01 and 0.02 cm. It is shown on Figure 4 as the blue-colored area (CRII). This region is almost free of prompt sources contamination. Its usage will become important in the QCD estimation, where only the excess over non-QCD MC data is used.

6.4 The Signal Regions

The Signal regions (SR) are the part of the d_0 spectrum, where the background density is very small. This area is then ideal to target, in order to look for displaced signatures. There are three SRs; SRI, SRII and SRIII. These are clearly shown in Figure 4 and differ in levels of signal to background ratio. They are also referred respectively as the Loose, Medium and Tight Signal region. The Loose SR starts at 0.05 cm, the Medium SR at 0.1 cm and the Tight SR at 1.0 cm. The final goal will consist of predicting the background number of events expected in these regions. However, the data in the SRs must be blinded, which prevents that one would be biased in the estimation by looking at the data.

As discussed, the non-QCD background will be estimated with the available MC samples of the different background processes after reliability check in the PCR. For QCD background, it will be slightly more complicated, one needs to define an additional control region, which is explained in the next section.

6.5 The $b\bar{b}$ control region

Unfortunately, QCD MC samples do not provide enough statistics to enable a simple MC-data agreement method to predict the background. This is why a data-driven method is used to do so. The strategy will be explained later in the next chapter, but the motivation of adding a control region follows from the necessity of finding QCD dominated regions. This will provide more information on the behavior of the d_0 spectrum from QCD-muons, which are expected to come from background decays. The $b\bar{b}$ Control region has in fact a different topology than the one assumed in Section 5.

In this case, the selection on the number of muons is relaxed to only one muon per event. This muon is expected to be produced in Bottom anti-

Bottom quark production ($b\bar{b}$), and is reconstructed as a jet, a consequence of hadronization. Tagging jets is a delicate task, where the algorithm makes usage of the d_0 of the reconstructed particles. In order to prevent biasing, one in the selection requires only one b -jet to be identified as a b -jet. The other jet (X-jet) is assumed to contain the muon, and this represents the topology assumed for the $b\bar{b}$ Control region. Because the muon is contained in the X-jet, only non-isolated muons are selected ($Iso > 0.15$), and must have an angular separation $\Delta R < 0.2$ with the X-jet. The two jets are assumed to be produced back-to-back, so,

$$\Delta\phi = |\phi_{X-jet} - \phi_{b-jet}| > 2.5, \quad (15)$$

where $\Delta\phi$ is the azimuthal angle difference between the jets. Further, the same requirements on p_T , η and identification of a real muon are applied (see Table 3). The obtained MC data-set is dominated by QCD-muons and is ready to be used for the QCD estimation. Note that the entire d_0 spectrum can be used here, since it does not overlap with the signal topology, so no blinding is applied in this case as no signal is expected.

6.6 The $\mu\mu$ non-isolated control region

A last set of control regions are defined, which are completely identical to those in 6.1, 6.2 and 6.3, with the exception that the two muons are required to be not isolated. These regions are used in a closure test, where the estimation method for QCD is tested, which is detailed in the Chapter 7.

7 Non-QCD background estimation

As mentioned previously, before getting started with the estimation of the number of events for the non-QCD background, one needs to check the validity of the MC w.r.t. the data, and this is done in the PCR defined in the previous chapter.

7.1 MC and data agreement in the Prompt Control Region

Initially, all the MC samples together have more events than the data. This has the advantage to have small uncertainties; the more data, the better the statistics. The first task is to normalize it to the corresponding integrated luminosity using the normalization factor of the different processes in equation 10. Every selected event of a certain process is then weighted with this

factor, which is different for the various processes and Runs. In Table 4, the values of integrated luminosity of the different Runs are listed. The cross sections of the considered process can be found in the following reference [12]. After normalization, the other corrections mentioned previously are applied.

Table 4: The integrated luminosity of the different Runs of taking data [4]

Integrated luminosity \mathcal{L} (pb^{-1})	
Run B	5868.83
Run C	2631.68
Run D	4339.14
Run E	4034.04
Run F	3160.08
Run G	7505.44
Run H	8152.88

One way to check the consistency between MC and data is to look at the invariant mass plot, where the Z-peak, representing the Z-boson mass, should be in agreement with the data. This plot is shown for Run H in Figure 5, where the invariant mass of the two muons in the PCR is plotted. The various colored MC histograms represents the contribution of the different processes to the background, while the black dots are the data. A ratio plot is presented below the histograms, in order to make the comparison easier. A flat ratio plot around unity proves the MC-data agreement. Natural units are used in this work, so the mass is given in GeV.

The ratio plot is clearly flat on average, which shows the agreement. Beside small statistical fluctuations around the tails, there is slight deviation from unity at the Z-peak. This is a known effect due to a difference in resolution between data and simulation [6], but the agreement is still within 90% which is acceptable. It is also clear from the plot that the Drell-Yan process is the most dominant background source among prompt sources. In the Appendix, in Table 5 the number of events of each background source is given for the different Runs, with the fraction of their contribution to the total background.

To check further the consistency with data, one can also plot distributions of the parameter defined in the previous chapter. These are shown in Figures 6 and 7, respectively for the p_t and d_0 of the two muons.

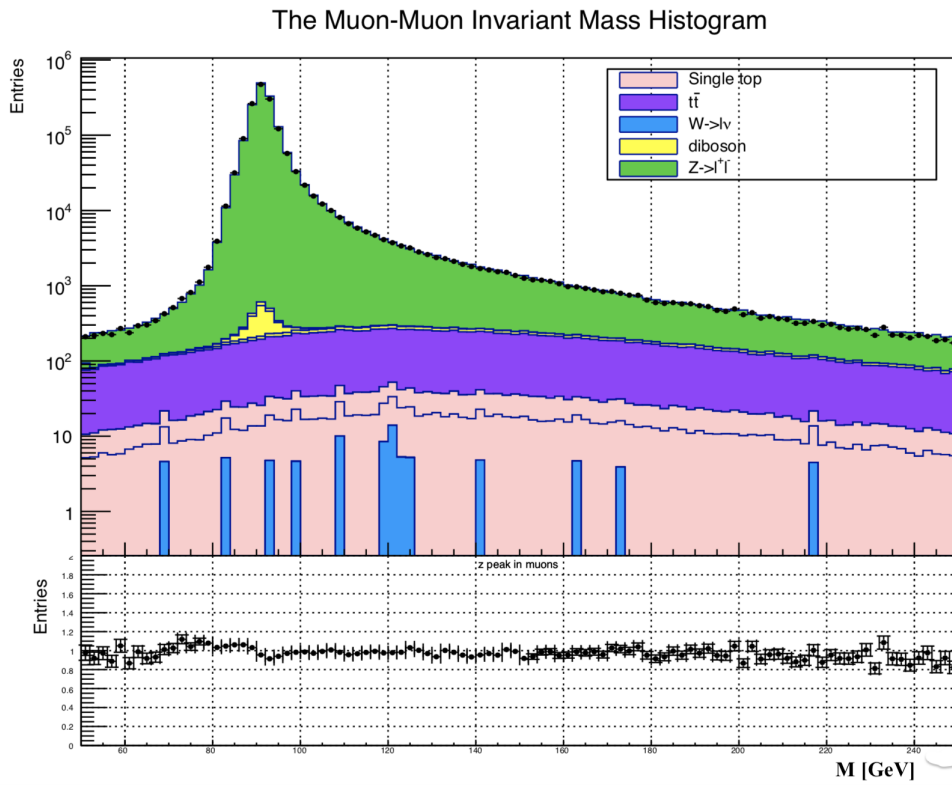


Figure 5: The invariant mass plot for muons in the PCR. The colored histograms represents the MC, while the black dots the data. A ratio plot is presented below the histograms, in order to make the comparison easier.

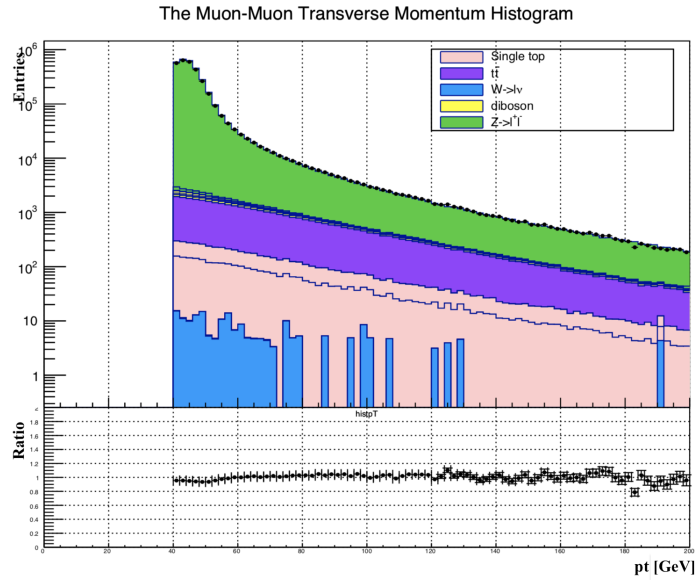


Figure 6: The transverse momentum plot for muons in the PCR. The colored histograms represents the MC, while the black dots the data.

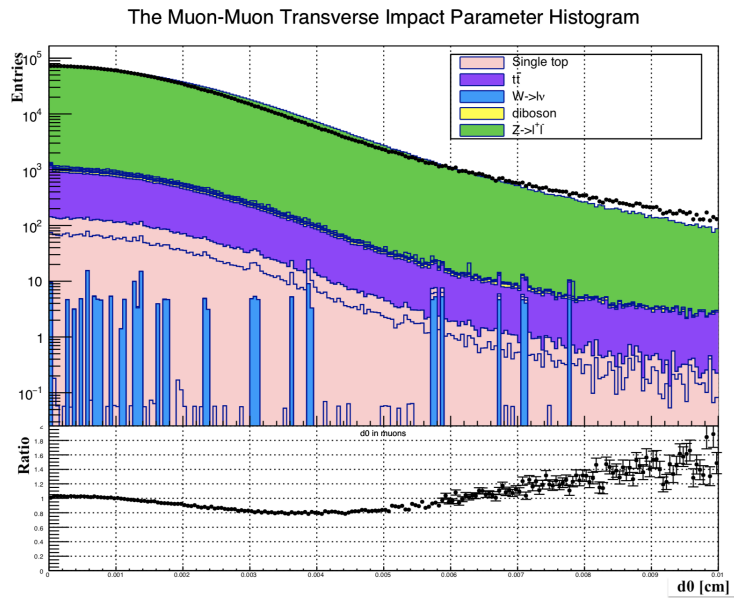


Figure 7: The transverse impact parameter plot for muons in the PCR. The colored histograms represents the MC, while the black dots the data.

The p_t plot (Figure 6) confirms again the MC-data agreement. Note that the distribution starts at 40 GeV, which is the value of the cut applied in the event selection.

However, the d_0 histogram is not matching very well. There are two explanations regarding this fact. The difference in MC and data in the low d_0 values is also due to differences in resolution between simulation and reconstruction. Luckily this effect is not important with an increasing d_0 . The discrepancy in the higher d_0 values can be explained from the absence of QCD contribution, which becomes dominant at an increasing d_0 and the QCD is derived from the data.

From the agreement obtained in these plots, one can trust the MC, in order to make further predictions of the non-QCD background. The results are presented in Chapter 10 with the QCD prediction, which is discussed in the next chapter.

8 QCD background estimation

As explained before, QCD events are harder to predict. One can not use MC samples to model the data, since the physics is poorly understood in order to make decent simulations. It is also computationally challenging to simulate a reasonable size of samples. This is why a different approach is considered to predict the QCD number of events in the Signal Regions.

8.1 Data-driven method

Two control regions were defined in Chapter 6.2 and 6.4; the Displaced Control Region and the $b\bar{b}$ Control Region. The purpose of these regions is to develop a method to predict the QCD background, without depending on QCD MC. The goal consists of estimating the number of event in the SRs, which are defined in the d_0 representation in Figure 4. The idea is to predict the number of QCD events by applying equation 11, where the well-understood non-QCD MC is subtracted from the data in control regions, assuming the remaining data is QCD. These QCD samples can then be used to determine the background in the SRs using the following method:

Assuming that the muons coming from QCD processes behave the same way, the QCD dominant $b\bar{b}$ Control Region has been defined to have a considerable number of QCD events. Because this region does not overlap with

the SRs, one can look at its full d_0 spectrum in the data without unblinding. Equation 11 applied to generate pure QCD samples for the different Runs. In Figure 8, the d_0 spectrum of the one muon in the $b\bar{b}$ Control Region is shown for Run C.

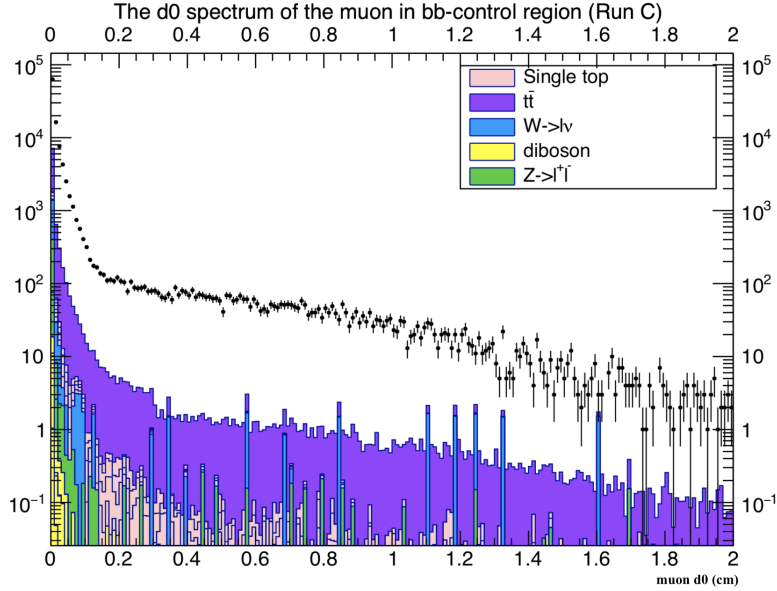


Figure 8: The d_0 spectrum of the one muon in the $b\bar{b}$ Control Region is shown for Run C. The colored histograms represents the MC, while the black dots the data. The gap between data and non-QCD MC is assigned to be the QCD contribution.

It is clear from the gap between data and non-QCD MC that this region is dominated by QCD background. Subtracting the non-QCD events in Figure 8 gives the QCD d_0 spectrum plotted in Figure 9. For the $b\bar{b}$ Control Region, there are QCD MC samples available. In Figure 9, the QCD MC is plotted (red histogram) with the QCD data. However these samples are only used to check the consistency in shape of the spectrum, and are not be used to model the data. In fact, the agreement in Figure 9 is obtained, not only with the previously discussed corrections on the MC, but the MC histograms has been also normalized to the number of events in the QCD data. Beside statistical fluctuations, the shape of the two histograms is very similar.

Having these QCD samples for all Runs, one can perform the data-driven method. The idea behind this method is the following; assuming QCD muons to have a similar behavior in the d_0 spectrum, one can calculate transfer fac-

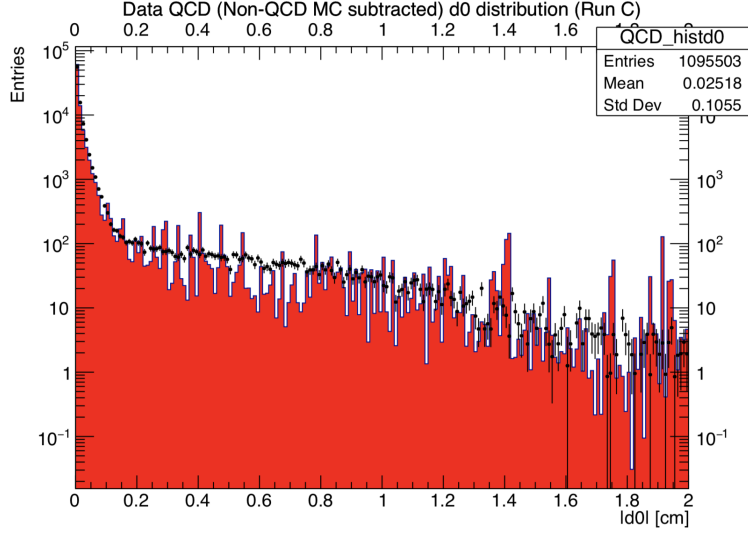


Figure 9: The QCD d_0 spectrum from data with non-QCD MC subtracted for Run C. The red distribution represents the QCD MC while the black dots the data.

tors $f_{\mu,i}$ defined as,

$$f_{\mu,i} = \frac{N_{d_0 > x_i}}{N_{0.01 < d_0 < 0.02}}, \quad \text{with } x_i \in \{0.02; 0.05; 0.1\} \quad (16)$$

where $N_{d_0 > x_i}$ is the number of events of the one-dimensional equivalent of the i -th SR and $N_{0.01 < d_0 < 0.02}$ of the DCR. Assuming similarity in shape, this ratio would be the same in two different QCD histograms. Therefore, one can calculate the transfer factors of a certain d_0 -histogram, and multiply these with $N_{0.01 < d_0 < 0.02}$ of another histogram to obtain $N_{d_0 > x_i}$ in this latter.

However, in the case where two muons are required in an event, one has to estimate number of events using a two-dimensional histogram. Thus in order to estimate $N_{SR,i}$ the number of events in the i -th SR (Chapter 6.3), using N_{DCR} (Chapter 6.2), the i -th transfer factor is multiplied twice, taking in account the two muons,

$$N_{SR,i}(QCD) = N_{DCR}(QCD) * f_{\mu,i}^2, \quad (17)$$

where the $f_{\mu,i}$ are calculated from the $b\bar{b}$ Control Region. Applying the transfer factor twice for two muons relies on predictions that make more assumptions than in the one-dimensional case. Therefore a closure test is performed to prove the reliability of the estimation method. This closure test also allows to determine the uncertainty of the prediction method.

8.2 Closure test for the data-driven method

In this section, the previously discussed method is tested, and for the sake of generality, a completely independent control region is used to prove its reliability. Therefore the $\mu\mu$ non-isolated control region has been defined in Section 6.5, where the samples contain non-isolated muons, making these orthogonal to the samples of interest from $\mu\mu$ isolated. Again, the complete data-set can be exploited because of orthogonality. Note that Figure 4 is applicable for this control region, so names such as DCR and SR are used to refer to the corresponding areas in the d_0 spectrum.

The strategy for testing the method will consist of defining random regions in the two dimensional d_0 spectrum of the non-isolated muons, and try to predict the number of events using transfer factors. The estimations can be then compared to numbers obtained by direct counting, in order to make further conclusions. In Figure 10, the two-dimensional d_0 histogram for QCD

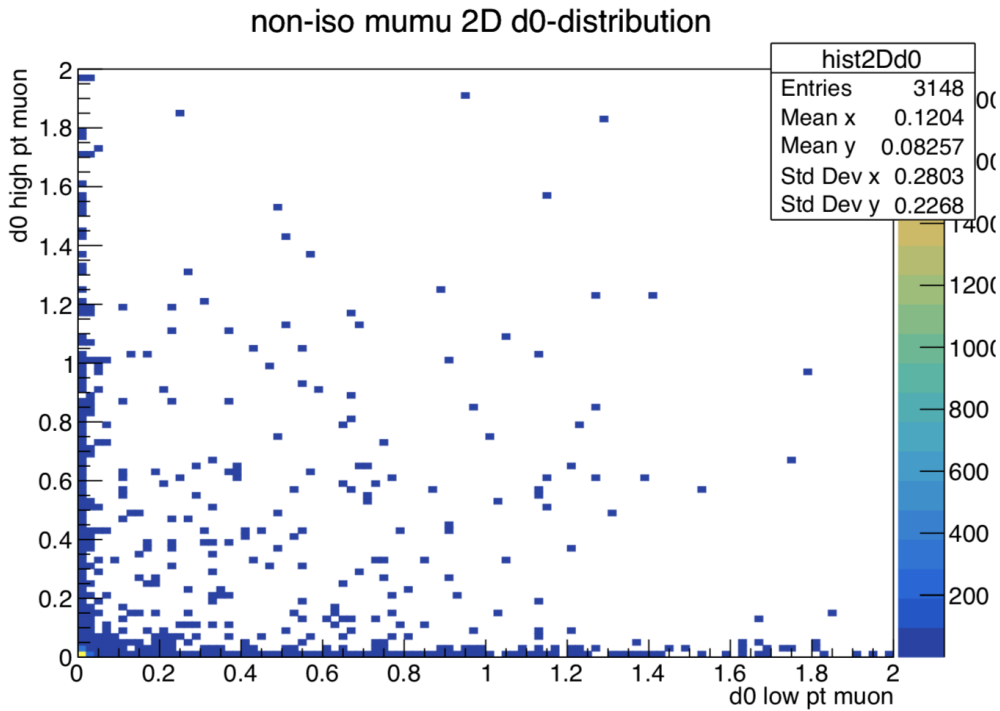


Figure 10: The QCD two-dimensional d_0 spectrum from data with non-QCD MC subtracted for Run C. On the x-axis one has the d_0 of the first muon and on the y-axis the d_0 of the second muon.

non-isolated muons is plotted for Run C. On the x-axis one has the d_0 of the

first muon and on the y -axis the d_0 of the second muon. However, muons on the different axes are not randomly distributed. In one interesting event, the muon with the lowest p_t value is always plotted on the x -axis while the one with the highest p_t value on the y -axis. This bias is assumed to have no considerable effect on the analysis.

Before doing the closure test, random sub-regions are defined in the half prompt- half displaced control regions, labeled as CRIII and CRIV in Figure 4. The closure test necessitates the definition of a normalization sub-region and a target sub-region. The former is used to multiply its number of events with the transfer factors, to predict the number of events in the target sub-region. In Figure 11, the sub-regions in the CRIII are shown, where the green rectangle represents the target region and the red one the normalization region. Note that the point (x, y) is shared by the two rectangles.

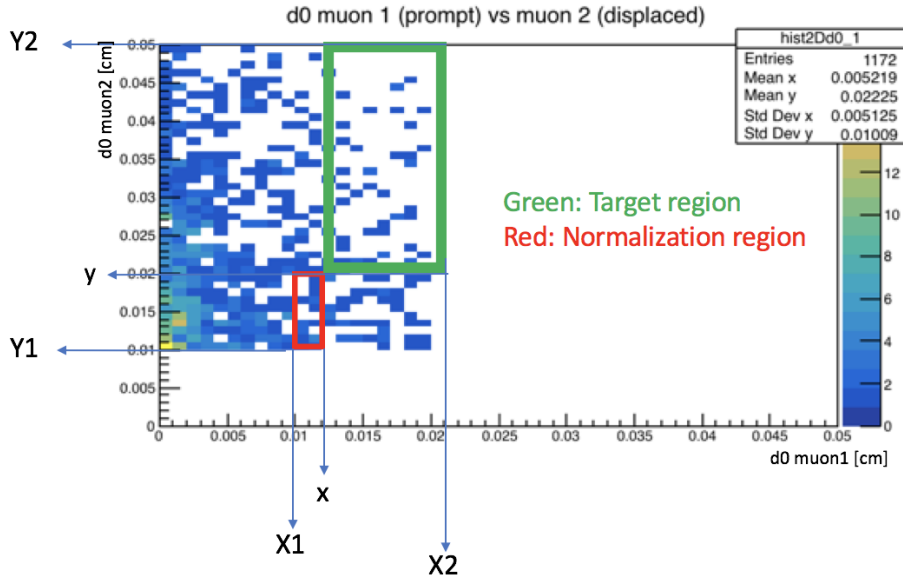


Figure 11: The QCD two-dimensional d_0 spectrum from non-isolated $\mu\mu$ data with non-QCD MC subtracted for Run C. On the x -axis one has the d_0 of the first muon and on the y -axis the d_0 of the second muon. The area within the green rectangle corresponds to the target region, while the red one is the normalization region.

Next task consists of calculating the two transfer factors, one along the x -axis

Table 5: The nine different (x,y) points are shown for the definition of the target and the normalization area in the CRIII and CRIV.

CRIV			
	y=0.012cm	y=0.015cm	y=0.018cm
x=0.02cm	(0.02,0.012)	(0.02,0.015)	(0.02,0.018)
x=0.025cm	(0.025,0.012)	(0.025,0.015)	(0.025,0.018)
x=0.03cm	(0.03,0.012)	(0.03,0.015)	(0.03,0.018)
CRIII			
	y=0.02cm	y=0.025cm	y=0.03cm
x=0.012cm	(0.012,0.02)	(0.012,0.025)	(0.012,0.03)
x=0.015cm	(0.015,0.02)	(0.015,0.025)	(0.015,0.03)
x=0.018cm	(0.018,0.02)	(0.018,0.025)	(0.018,0.03)

and another one along the y-axis. Analogously to equation 16, one has,

$$f_{\mu,x} = \frac{\int_x^{X2} d_0(\mu_1)}{\int_{X1}^x d_0(\mu_1)}, \quad (18)$$

$$f_{\mu,y} = \frac{\int_y^{Y2} d_0(\mu_2)}{\int_{Y1}^y d_0(\mu_2)}, \quad (19)$$

where in both equation, the nominator represent the integral of the target region along the x-axis in Equation 18, and the y-axis in Equation 19. Similarly, the denominator corresponds to the normalization region. Finally the closure test is performed using the following equation,

$$N_{target} = N_{normalization} * f_{\mu,x} * f_{\mu,y}, \quad (20)$$

where N is the number of events. After calculating N_{target} , one can compare the result to the number obtained from simply counting events in the target region. If the two number are consistent, then the method can be trusted to use it for the QCD estimation in the $\mu\mu$ isolated SRs.

This procedure is repeated for nine different configurations, by simply moving the shared point between the two rectangles (x,y). In addition, the same closure test is repeated for the CRIV, shown in Figure 12.

In Table 6, the nine different (x,y) points are shown for the definition of the target and the normalization area in the CRIII and CRIV. The results of the closure test for Run D are given in Figure 13 and 14. In these tables, the second column represents the number of events in the target region

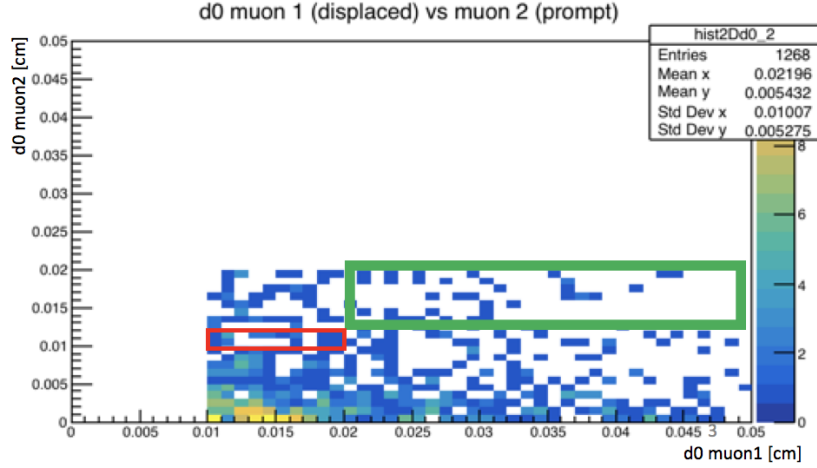


Figure 12: The QCD two-dimensional d_0 spectrum from non-isolated $\mu\mu$ data with non-QCD MC subtracted for Run C. On the x-axis one has the d_0 of the first muon and on the y-axis the d_0 of the second muon. The area within the green rectangle corresponds to the target region, while the red one is the normalization region.

calculated with Equation 20. The third one shows the number obtained by simple counting the number of events in the target region. Finally the last column shows the agreement between the two numbers, where a value close to unity within the uncertainty confirms the agreement. The uncertainties are calculated with propagation of uncertainty of the three parameters in Equation 20.

The same is repeated for all Runs, in Figure 15 the average is taken for the nine configurations in the CRIII and CRIV for each Run. It is clear from these numbers that the closure test has successfully validated the method. The agreement is obtained almost in every region for all Runs. The data-driven method is now ready to be used for the estimation of QCD number of events in SRs.

	Data-driven method	Direct counting	Ratio
y=0.012cm;x=0.02cm	275.271 +/- 58.036	181.228 +/- 13.64	1.5189 +/- 0.435
y=0.012cm;x=0.025cm	103.836 +/- 20.246	83.774 +/- 9.275	1.2395 +/- 0.379
y=0.012cm;x=0.03cm	42.079 +/- 9.643	28.018 +/- 5.386	1.5019 +/- 0.633
y=0.015cm;x=0.02cm	233.605 +/- 47.674	164.11 +/- 12.963	1.4235 +/- 0.403
y=0.015cm;x=0.025cm	91.673 +/- 17.386	75.197 +/- 8.776	1.2191 +/- 0.373
y=0.015cm;x=0.03cm	36.792 +/- 8.292	27.248 +/- 5.292	1.3503 +/- 0.567
y=0.018cm;x=0.02cm	205.175 +/- 41.302	139.792 +/- 11.96	1.4677 +/- 0.421
y=0.018cm;x=0.025cm	83.178 +/- 15.575	65.456 +/- 8.187	1.2708 +/- 0.397
y=0.018cm;x=0.03cm	33.627 +/- 7.516	24.342 +/- 5.001	1.3814 +/- 0.593

Figure 13: The closure test for testing the data-driven method in the CRIII for Run D. The second column represents the number of events in the target region calculated with Equation 20. The third one shows the number obtained by simple counting in the target region. Finally the last column shows the agreement between the two numbers, where a value close to unity within the uncertainty confirms the agreement.

	Data-driven method	Direct counting	Ratio
x=0.012cm;y=0.02cm	154.115 +/- 34.941	146.748 +/- 12.331	1.0502 +/- 0.326
x=0.012cm;y=0.025cm	146.522 +/- 31.354	129.619 +/- 11.578	1.1304 +/- 0.343
x=0.012cm;y=0.03cm	139.071 +/- 28.839	114.084 +/- 10.865	1.219 +/- 0.369
x=0.015cm;y=0.02cm	65.472 +/- 13.473	52.583 +/- 7.418	1.2451 +/- 0.432
x=0.015cm;y=0.025cm	59.084 +/- 11.845	50.0 +/- 7.213	1.1817 +/- 0.407
x=0.015cm;y=0.03cm	54.376 +/- 10.75	43.23 +/- 6.71	1.2578 +/- 0.444
x=0.018cm;y=0.02cm	35.191 +/- 8.098	25.936 +/- 5.197	1.3568 +/- 0.584
x=0.018cm;y=0.025cm	30.732 +/- 6.967	25.118 +/- 5.1	1.2235 +/- 0.526
x=0.018cm;y=0.03cm	28.586 +/- 6.417	22.235 +/- 4.797	1.2856 +/- 0.566

Figure 14: The closure test for testing the data-driven method in the CRIV for Run D. The second column represents the number of events in the target region calculated with Equation 20. The third one shows the number obtained by simple counting in the target region. Finally the last column shows the agreement between the two numbers, where a value close to unity within the uncertainty confirms the agreement.

Run	Mean agreement CRIII	Mean agreement CRIV
B	1.011 +/- 0.367	1.021 +/- 0.353
C	1.004 +/- 0.437	1.024 +/- 0.421
D	1.217 +/- 0.444	1.375 +/- 0.467
E	0.899 +/- 0.316	1.207 +/- 0.393
F	1.054 +/- 0.390	1.081 +/- 0.344
G	0.991 +/- 0.363	0.988 +/- 0.349
H	1.110 +/- 0.232	1.283 +/- 0.281

Figure 15: The mean agreement for the closure test in CRIII and CRIV for all Runs.

8.3 QCD estimation in the Signal Regions

As discussed in Chapter 8.1, the transfer factors used for the QCD estimation in the SRs are calculated from the $b\bar{b}$ Control Region, where the full d_0 spectrum can be exploited. The normalization region used in this case is the $\mu\mu$ isolated DCR, because the QCD contribution is more significant in comparison to the PCR, where the prompt sources contamination is very important, as seen in Table 5. The transfer factors calculated with Equation 16 from the $b\bar{b}$ Control Region for the different Runs are listed on Figure 16. From these numbers, one can conclude that the transfer factors are relatively

Transfer factors calculated from BEnriched Non-iso (bbar + mu)			
Run's	TF1 (SR1)	TF2 (SR2)	TF3 (SR3)
B	1.417 +/- 0.017	0.533 +/- 0.008	0.277 +/- 0.005
C	1.517 +/- 0.022	0.631 +/- 0.012	0.361 +/- 0.008
D	1.386 +/- 0.018	0.534 +/- 0.009	0.293 +/- 0.006
E	1.341 +/- 0.021	0.513 +/- 0.011	0.291 +/- 0.007
F	1.345 +/- 0.022	0.522 +/- 0.011	0.293 +/- 0.007
G	1.058 +/- 0.012	0.256 +/- 0.005	0.047 +/- 0.002
H	1.061 +/- 0.009	0.256 +/- 0.003	0.052 +/- 0.001

Figure 16: Transfer factors calculated with Equation 16 from the $b\bar{b}$ Control Region, used in the estimation of QCD.

similar from Run B to Run F. However, Run G and H seems to be different. This would imply that the QCD d_0 spectrum in $b\bar{b}$ Control Region of these last Runs has a different shape w.r.t. the other Runs. There are in fact differences between Run G and H, and the other Runs. The high instantaneous luminosity during these Runs led to problems in the readout electronics of the tracker. A consequence of this issue was the drop of the isolation, identification, reconstruction and trigger efficiencies for muons, which is needed in this analysis for the corrections applied on the MC. Therefore these are provided separately for these two Runs.

The remaining difference is expected to be the cause of this incompatibility. For instance, one could perform the analysis, by merging all the Runs together, which is also statistically and technically advantageous, but due

to the differences in the Runs, every data-set is analyzed separately. This decision can be supported by looking to the data from the different Runs in the $b\bar{b}$ Control Region, shown in Figure 17. It can be seen that Run G and H are not matching the others curves. However, analyzing the different Runs separately has the advantage to enable comparison of results obtained from the different Runs.

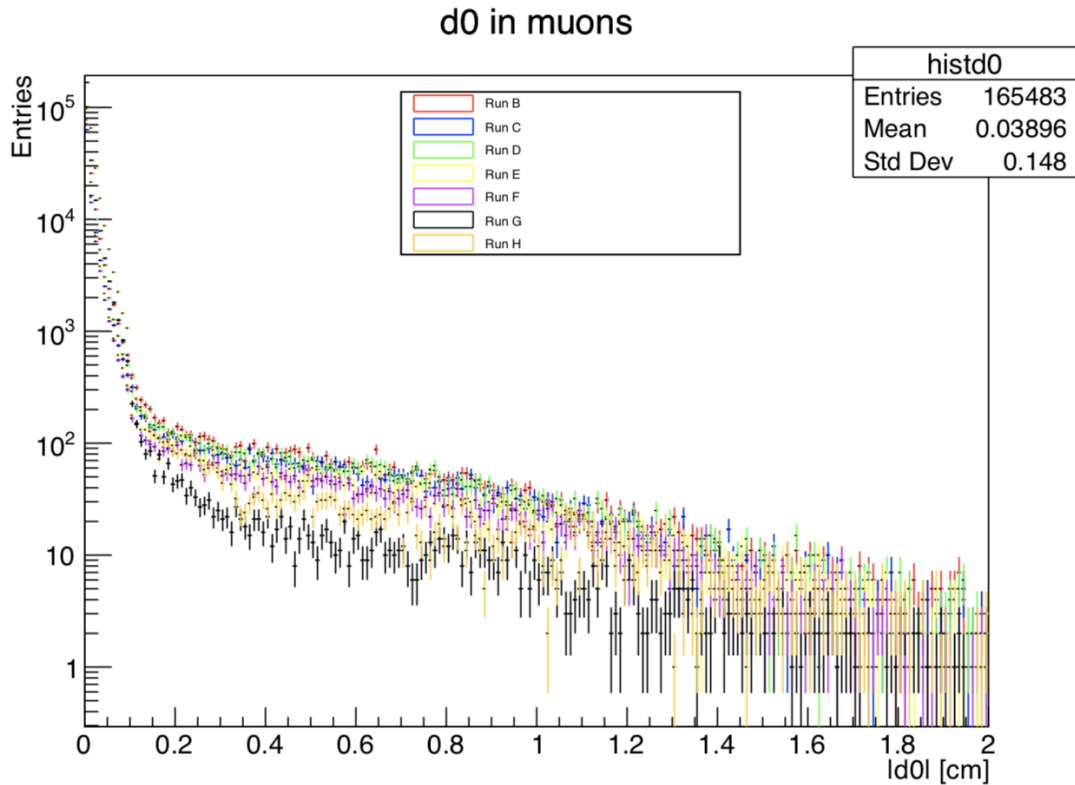


Figure 17: Comparison of data in the $b\bar{b}$ Control Region for the different Runs. Clearly, Run G and H shows a deviation from the other Runs.

9 Background estimation results

9.1 QCD background

Using the transfer factors listed in Figure 16, the QCD contribution calculated with Equation 16 in the $\mu\mu$ isolated SRs is shown in Table 7 and 8, for the three SRs and for all Runs. The number of events in the DCR (the

Table 6: QCD number of events in the Signal Regions calculated with Equation 16, for Run B, C and D. The corresponding number of events in de the Displaced Control Region are also given.

Runs	B	C	D
N_{DCR}	-1.668 ± 0.429	4.665 ± 2.238	8.088 ± 3.009
N_{SR1}	0.001 ± 0.4323	10.735 ± 5.155	15.538 ± 5.788
N_{SR2}	0.001 ± 0.0691	1.857 ± 0.893	2.306 ± 0.86
N_{SR3}	0.001 ± 0.0229	0.608 ± 0.292	0.694 ± 0.259

Table 7: QCD number of events in the Signal Regions calculated with Equation 16, for Run E, F, G and H. The corresponding number of events in de the Displaced Control Region are also given.

Runs	E	F	G	H
N_{DCR}	4.212 ± 2.245	5.516 ± 2.453	12.273 ± 3.936	22.782 ± 5.166
N_{SR1}	7.575 ± 4.041	9.979 ± 4.443	13.737 ± 4.411	25.646 ± 5.823
N_{SR2}	1.108 ± 0.592	1.503 ± 0.67	0.804 ± 0.259	1.493 ± 0.339
N_{SR3}	0.357 ± 0.191	0.474 ± 0.211	0.027 ± 0.009	0.062 ± 0.014

normalization region in this case) N_{DCR} is also given, which represents the QCD contribution, obtained by subtracting the non-QCD MC from the data.

For Run B, this number of events is confusing; the N_{DCR} is negative. This means the following: when subtracting the non-QCD MC from the data using Equation 11, the MC seems to exceed the data on average, leading to a negative value. The result for QCD contribution in the DCR for Run B is set to 0.001 to keep it physical.

Moreover, the statistics in the $\mu\mu$ isolated DCR are very poor. This can be seen for example in p_t histogram for Run E in Figure 18. Due to this lack of statistics, QCD estimated number of events have larger relative uncertainties.

Beside Run B, the numbers got from the other Runs seems to be relatively close to each other. This is even case for Run G and H, where the small transfer factors are compensated by the larger N_{DCR} , because of the higher luminosity, and thus more statistics.

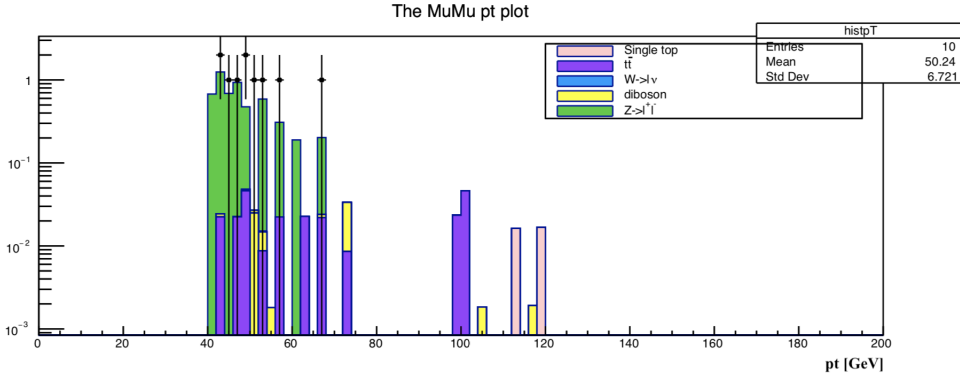


Figure 18: The p_t distribution in the Displaced Control Region for isolated $\mu\mu$ for Run E. This plots shows the very poor statistics in the Displaced Control Region, were very few QCD events can be collected.

9.2 Non-QCD Background

In Section 7, the non-QCD MC has been used to model the data in the Prompt Control Region, where the QCD was expected to have no significant contribution, which makes it a good control region for non-QCD. After the application of several corrections to the MC, the agreement with the data was finally obtained. This check was important in order to trust the MC, and use it further for non-QCD background estimation in the SRs, where the data are blinded. One can now count number of events from the MC in the SRs and estimate the background contribution. The results of the non-QCD background from the different processes mentioned in Chapter 4.2.1 are listed in Table 9 for all Runs.

From these results, it is clear that the non-QCD contribution in the SRs is very low. As expected, the number of events of the background is reduced as the SR becomes tighter. One can also see that results from different Runs are close to each other, where Run G and H are showing slightly high event numbers due to their high luminosity.

10 Supersymmetric Top Quark Monte Carlo Estimation

As mentioned in the introduction, the analysis performed in this thesis can be considered for any model predicting two muons in the final state, satisfying the requirements of selection listed in Table 3. As an example model

Table 8: The non-QCD background estimation of the different processes in the $\mu\mu$ isolated Signal Regions obtained from MC for all Runs.

Run	Process	SR1	SR2	SR3
B	$Z \rightarrow \mu\mu$	1.409 ± 0.097	0.945 ± 0.079	0.705 ± 0.068
	Diboson	0.008 ± 0.004	0.003 ± 0.002	0.001 ± 0.001
	$t\bar{t}$	0.161 ± 0.013	0.071 ± 0.009	0.049 ± 0.007
	Singletop	0.013 ± 0.004	0.006 ± 0.003	0.003 ± 0.001
	$W \rightarrow \mu\nu$	0.052 ± 0.007	0.037 ± 0.006	0.023 ± 0.005
C	$Z \rightarrow \mu\mu$	0.283 ± 0.02	0.19 ± 0.016	0.142 ± 0.014
	Diboson	0.002 ± 0.001	0.001 ± 0.0	0.0 ± 0.0
	$t\bar{t}$	0.032 ± 0.003	0.014 ± 0.002	0.01 ± 0.001
	Singletop	0.003 ± 0.001	0.001 ± 0.001	0.001 ± 0.0
	$W \rightarrow \mu\nu$	0.023 ± 0.003	0.016 ± 0.003	0.01 ± 0.002
D	$Z \rightarrow \mu\mu$	0.77 ± 0.053	0.516 ± 0.043	0.386 ± 0.037
	Diboson	0.004 ± 0.002	0.001 ± 0.001	0.0 ± 0.0
	$t\bar{t}$	0.088 ± 0.007	0.039 ± 0.005	0.027 ± 0.004
	Singletop	0.007 ± 0.002	0.003 ± 0.001	0.002 ± 0.001
	$W \rightarrow \mu\nu$	0.039 ± 0.005	0.027 ± 0.004	0.017 ± 0.003
E	$Z \rightarrow \mu\mu$	0.666 ± 0.046	0.446 ± 0.037	0.333 ± 0.032
	Diboson	0.004 ± 0.002	0.001 ± 0.001	0.0 ± 0.0
	$t\bar{t}$	0.076 ± 0.006	0.033 ± 0.004	0.023 ± 0.003
	Singletop	0.006 ± 0.002	0.003 ± 0.001	0.002 ± 0.001
	$W \rightarrow \mu\nu$	0.036 ± 0.005	0.025 ± 0.004	0.016 ± 0.003
F	$Z \rightarrow \mu\mu$	0.409 ± 0.028	0.274 ± 0.023	0.205 ± 0.02
	Diboson	0.002 ± 0.001	0.001 ± 0.001	0.0 ± 0.0
	$t\bar{t}$	0.047 ± 0.004	0.02 ± 0.002	0.014 ± 0.002
	Singletop	0.004 ± 0.001	0.002 ± 0.001	0.001 ± 0.0
	$W \rightarrow \mu\nu$	0.028 ± 0.004	0.02 ± 0.003	0.012 ± 0.002
G	$Z \rightarrow \mu\mu$	2.302 ± 0.159	1.543 ± 0.129	1.149 ± 0.11
	Diboson	0.013 ± 0.006	0.004 ± 0.003	0.002 ± 0.001
	$t\bar{t}$	0.265 ± 0.021	0.116 ± 0.014	0.08 ± 0.012
	Singletop	0.021 ± 0.006	0.01 ± 0.004	0.005 ± 0.002
	$W \rightarrow \mu\nu$	0.067 ± 0.009	0.047 ± 0.008	0.029 ± 0.006
H	$Z \rightarrow \mu\mu$	2.716 ± 0.187	1.82 ± 0.152	1.355 ± 0.13
	Diboson	0.016 ± 0.007	0.005 ± 0.004	0.002 ± 0.002
	$t\bar{t}$	0.313 ± 0.025	0.137 ± 0.017	0.095 ± 0.014
	Singletop	0.025 ± 0.007	0.012 ± 0.005	0.006 ± 0.003
	$W \rightarrow \mu\nu$	0.073 ± 0.01	0.051 ± 0.008	0.032 ± 0.006

Table 9: The different available MC samples for stops with different masses and lifetimes.

Available masses and lifetimes from the MC samples of stop quark production											
		Mass in (GeV)									
		200	300	400	500	600	700	800	1000	1100	1200
Lifetime $c\tau$ (mm)	1	x	x	x	x	x	x	x	x	x	x
	10	x	x	x	x	x	x	x	x	x	x
	100	x	x	x	x	x	x	x	x	x	x
	1000	x	x	x	x	x	x	x	x	x	x

for the motivation, the production of a pair of supersymmetric top quarks, having a considerable lifetime was considered, which are expected to decay in two opposite charged leptons and bottom quarks (see Chapter 2.3.1). A schematic representation of this process can be seen in Figure 1.

For this scenario, there are also MC samples available which can be exploited in order to check the model. These samples has been generated by the MC generator *PYTHIA* [7]. There are several samples predicting different masses and lifetimes of the stop particles. In Table 10, all the masses and lifetimes considered are listed. The production cross section for the different stop masses and lifetimes can be found in the following reference [12].

In order to check the model, a similar procedure is performed as for the prediction of the non-QCD background. The goal consists of estimating the number of events w.r.t. to the corresponding data luminosity of the Runs. This MC normalization is analogously calculated with Equation 10. Also corrections mentioned in Chapter 4.2.1 are applied on the signal samples.

After application of the necessary corrections, one can look to the d_0 -spectrum of the two muons, produced by the long-lived stops. It should be clear from the data-MC agreement obtained in the Prompt Control Regions of all Runs, that the signal contribution in that latter region will be negligible in comparison to the non-QCD background. Therefore the Signal regions were defined, where one would expect the signal to has a significant amount of events w.r.t. to the small background. In Figure 19, the d_0 -spectrum of muons produced from stops with a mass of 200 GeV and a lifetime $c\tau = 100$ mm, is shown for Run F. This has been repeated for all Runs and the results can be found in the Appendix.

It is clear from this plot that the stop contribution in the SRs would consid-

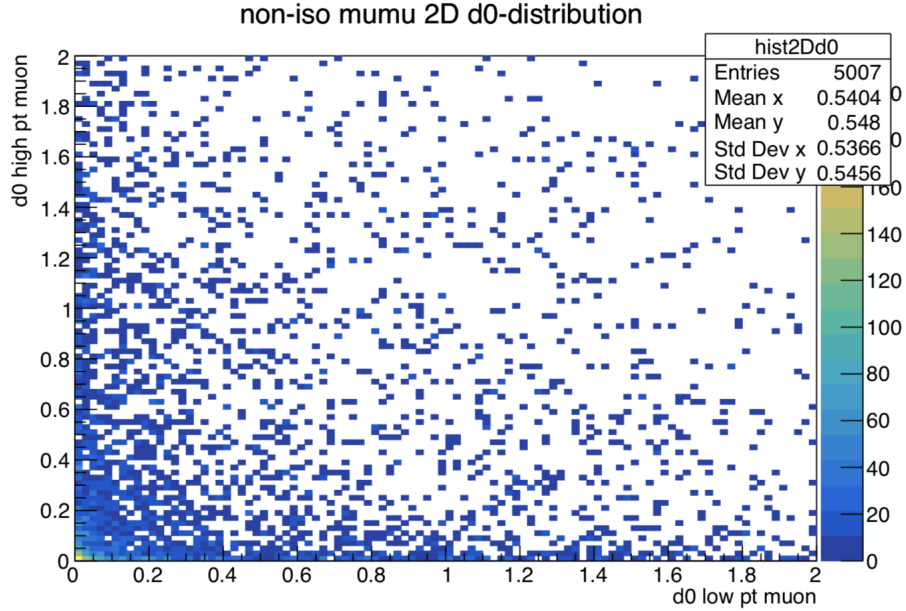


Figure 19: The d_0 -spectrum for stops with a mass of 200 GeV and a lifetime $c\tau = 100$ mm for Run F.

erably be larger than the background. From samples with the other lifetimes, one can conclude that the d_0 -spectrum is strongly correlated to the lifetime of the stop. The longer the lifetime, the higher the number of events of muons with higher d_0 . This can be clarified by looking to the d_0 -spectrum (Figure 20) of the stop with the same mass and shorter lifetime (1 mm). It is clear that most of events are concentrated in the control regions. Regarding the mass of the stop, there is no obvious correlation with the d_0 of the muons. The difference is manifested in the p_t -spectrum, where a higher mass corresponds to higher number of events for muons with a higher p_t .

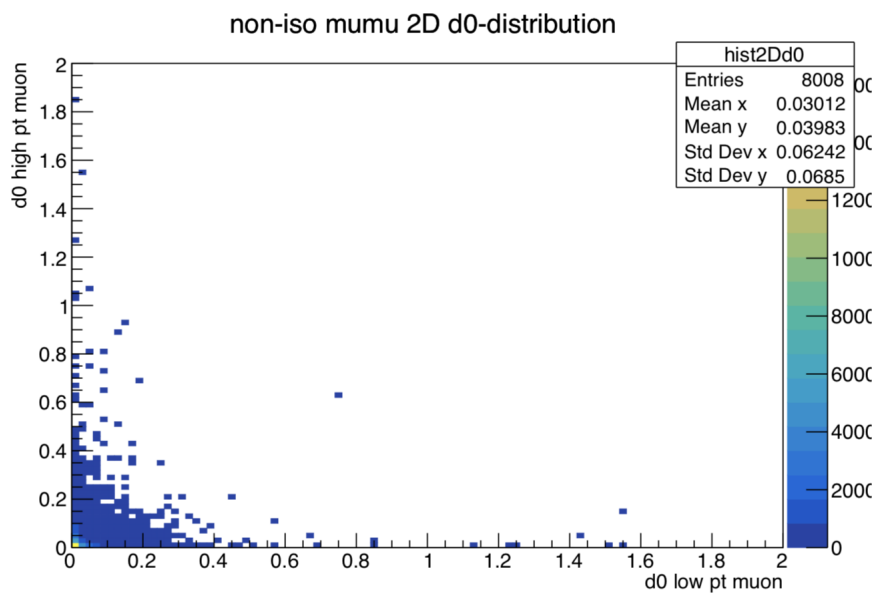


Figure 20: The d_0 -spectrum for stops with a mass of 200 GeV and a lifetime $c\tau = 1$ mm for Run F.

In Table 11, the number of events for all samples with different masses and lifetimes listed in Table 10, and are given in the three SRs for Run D. One can see that the low mass samples predicts larger numbers. This would have been observed if it was the case. So obviously, some of them are automatically excluded. Also it is clear that as the mass becomes larger, the number of events become smaller. For example a stop with a mass of 1200 GeV seems to have a very low cross section at the current center-of-mass energy of 13 TeV. This means also that no conclusions can be made on samples where the contribution is lower than the estimated background. Finally for the lifetime, samples with the first value in $c\tau$ (1 mm) will have mostly muons in the control regions, as seen in Figure 20. This is also why the number of events at 1 mm is always lower in SRs. For 10 and 100 mm, the expectation is higher in the SRs and finally when the stops decay too far (1000 mm), the number of events drops once again in the SRs, which is due to the constrained SRs.

Table 10: The signal estimation for $\mu\mu$ isolated in the Signal Regions obtained from MC for Run D.

stop t	SR1	SR2	SR3
200 GeV 1000 mm	1861.541 \pm 78.42	1597.556 \pm 72.483	1335.989 \pm 66.516
200 GeV 100 mm	12853.731 \pm 207.981	11296.736 \pm 195.209	9752.502 \pm 181.53
200 GeV 10 mm	16217.481 \pm 232.98	11678.607 \pm 197.698	7604.931 \pm 159.377
200 GeV 1 mm	4588.781 \pm 123.154	1161.563 \pm 62.007	219.522 \pm 26.799
300 GeV 1000 mm	328.474 \pm 12.081	285.772 \pm 11.272	244.521 \pm 10.414
300 GeV 100 mm	2200.11 \pm 31.048	1921.54 \pm 29.009	1658.675 \pm 26.952
300 GeV 10 mm	2493.55 \pm 33.051	1801.495 \pm 28.08	1168.253 \pm 22.595
300 GeV 1 mm	772.886 \pm 18.522	207.521 \pm 9.584	43.729 \pm 4.432
400 GeV 1000 mm	84.944 \pm 2.831	73.181 \pm 2.628	62.861 \pm 2.439
400 GeV 100 mm	520.732 \pm 7.068	461.07 \pm 6.654	395.958 \pm 6.168
400 GeV 10 mm	583.394 \pm 7.426	422.728 \pm 6.327	278.577 \pm 5.14
400 GeV 1 mm	178.016 \pm 4.11	48.082 \pm 2.14	10.797 \pm 1.018
500 GeV 1000 mm	28.563 \pm 0.874	24.882 \pm 0.817	21.498 \pm 0.76
500 GeV 100 mm	155.525 \pm 2.046	136.633 \pm 1.917	116.777 \pm 1.773
500 GeV 10 mm	172.425 \pm 2.165	124.139 \pm 1.836	80.356 \pm 1.478
500 GeV 1 mm	52.619 \pm 1.183	12.619 \pm 0.579	2.767 \pm 0.272
600 GeV 1000 mm	10.21 \pm 0.304	8.535 \pm 0.278	7.526 \pm 0.262
600 GeV 100 mm	54.106 \pm 0.698	47.974 \pm 0.658	41.276 \pm 0.61
600 GeV 10 mm	58.4 \pm 0.726	41.655 \pm 0.612	26.755 \pm 0.491
600 GeV 1 mm	17.5 \pm 0.396	4.252 \pm 0.196	0.7 \pm 0.08
700 GeV 1000 mm	4.176 \pm 0.12	3.618 \pm 0.112	3.109 \pm 0.104
700 GeV 100 mm	20.322 \pm 0.265	18.05 \pm 0.25	15.432 \pm 0.231
700 GeV 10 mm	21.771 \pm 0.274	15.634 \pm 0.232	10.033 \pm 0.186
700 GeV 1 mm	6.544 \pm 0.151	1.693 \pm 0.077	0.279 \pm 0.031
800 GeV 1000 mm	1.825 \pm 0.052	1.577 \pm 0.048	1.342 \pm 0.044
800 GeV 100 mm	8.827 \pm 0.114	7.892 \pm 0.108	6.796 \pm 0.1
800 GeV 10 mm	9.341 \pm 0.117	6.64 \pm 0.099	4.14 \pm 0.078
800 GeV 1 mm	2.844 \pm 0.064	0.686 \pm 0.032	0.138 \pm 0.014
1000 GeV 1000 mm	0.399 \pm 0.011	0.348 \pm 0.011	0.302 \pm 0.01
1000 GeV 100 mm	1.866 \pm 0.024	1.658 \pm 0.023	1.43 \pm 0.021
1000 GeV 10 mm	1.94 \pm 0.025	1.374 \pm 0.021	0.881 \pm 0.017
1000 GeV 1 mm	0.585 \pm 0.014	0.141 \pm 0.007	0.025 \pm 0.003
1100 GeV 1000 mm	0.201 \pm 0.006	0.174 \pm 0.005	0.15 \pm 0.005
1100 GeV 100 mm	0.918 \pm 0.012	0.814 \pm 0.011	0.692 \pm 0.011
1100 GeV 10 mm	0.956 \pm 0.012	0.671 \pm 0.01	0.416 \pm 0.008
1100 GeV 1 mm	0.279 \pm 0.007	0.07 \pm 0.003	0.011 \pm 0.001
1200 GeV 1000 mm	0.112 \pm 0.003	0.097 \pm 0.003	0.085 \pm 0.003
1200 GeV 100 mm	0.487 \pm 0.006	0.433 \pm 0.006	0.375 \pm 0.006
1200 GeV 10 mm	0.489 \pm 0.006	0.341 \pm 0.005	0.211 \pm 0.004
1200 GeV 1 mm	0.142 \pm 0.003	0.034 \pm 0.002	0.007 \pm 0.001

11 Limits on the SUSY model

The major goal of this analysis was to obtain the background contribution in the SRs where new physics signals would appear with a minimal background contamination. The results were given in Chapter 8, where the QCD and non-QCD estimation was approached differently. In the last chapter, the previously discussed SUSY model was simulated and the expected number of event in the SRs were estimated, listed in Table 11 for Run D. This has been repeated for all Runs, which can be found in the Appendix.

Having these number one can calculate limits on the model in function of the mass and the lifetime. These limits show which samples can be excluded, assuming no excess over the estimated background. For the calculation of the limits, one needs to include systematic uncertainties.

11.1 Systematic uncertainties on the background estimation

The systematic uncertainties can be assigned to the signal estimation, the non-QCD and the QCD background estimation. In the signal and non-QCD background, which were estimated using the MC, one can calculate the systematic uncertainties from the identification and the isolation scale factor. This can be done by running the entire analysis for the different scale factors,

$$f_{iso} + \sigma, f_{ID} + \sigma \quad \text{and} \quad f_{iso} - \sigma, f_{ID} - \sigma, \quad (21)$$

where σ is the standard deviation on the corresponding scale factor.

For QCD estimation, the systematic uncertainties can be obtained from the transfer factors, discussed Chapter 8.1. As mentioned before, the transfer factors were obtained from a completely different control region, the $b\bar{b}$ Control Region. For the selection of QCD events in this region, the decision was made that only one QCD jet was tagged as a B-jet. the motivation behind this was to minimize the d_0 -correlation in these samples, in order to avoid biasing. However, there are different levels on the requirements for the identification of a B-jet, depending on the B-tagging efficiency of the working point[6]. The different levels in the sternness on the working points are referred as; *loose*, *medium* and *tight* working points. Because this efficiency is d_0 -dependent, one can expect the transfer factors to be affected depending on the working point. For the transfer factors calculated in Chapter 8.3, a medium working point was used.

To calculate the systematic uncertainty on this decision for the calculation of the transfer factors, one can use the other working points to calculate the transfer factors again. Having these transfer factors, the following relative uncertainty can be calculated,

$$\frac{\max(f_{loose}, f_{medium}, f_{tight}) - \min(f_{loose}, f_{medium}, f_{tight})}{\text{mean}(f_{loose}, f_{medium}, f_{tight})}, \quad (22)$$

where the minimum of the three transfer factors is subtracted from the maximum, and the difference divided by the mean. Having the systematic uncertainties, one can calculate limits on the SUSY model, discussed in the next chapter.

11.2 Limit setting

If the background estimation in SRs obtained in this analysis is in agreement with the data, one can exclude several model predicting higher number of events over the background. This can be summarized in a limit plot, which is obtained by performing a hypothesis test using 95% confidence level, explained in [6]. The limit plot takes in account the background and the signal yields in all the SRs.

For each Run, a limit plot is calculated, shown in Figures 21 - 27. This typical plot is known as the exclusion contour plot, where the black dashed line represents the upper limit for the production cross section of the stops at 13 TeV with a $\mu\mu$ final state. The green band corresponds to the one σ deviation, while the yellow band two σ . This means that all samples with a corresponding mass and lifetime in the region on the left of the expected limit are excluded.

Comparing the results obtained from the different Runs, one can conclude that on average the limits are close to each other. However, it can be seen that Run G and H, has a slightly higher limit, which can be understood from their higher integrated luminosity in comparison to the other Runs, which has the advantage in the amount of statistics. Also Run B has a higher luminosity and it is clear that its limit is best after G and H.

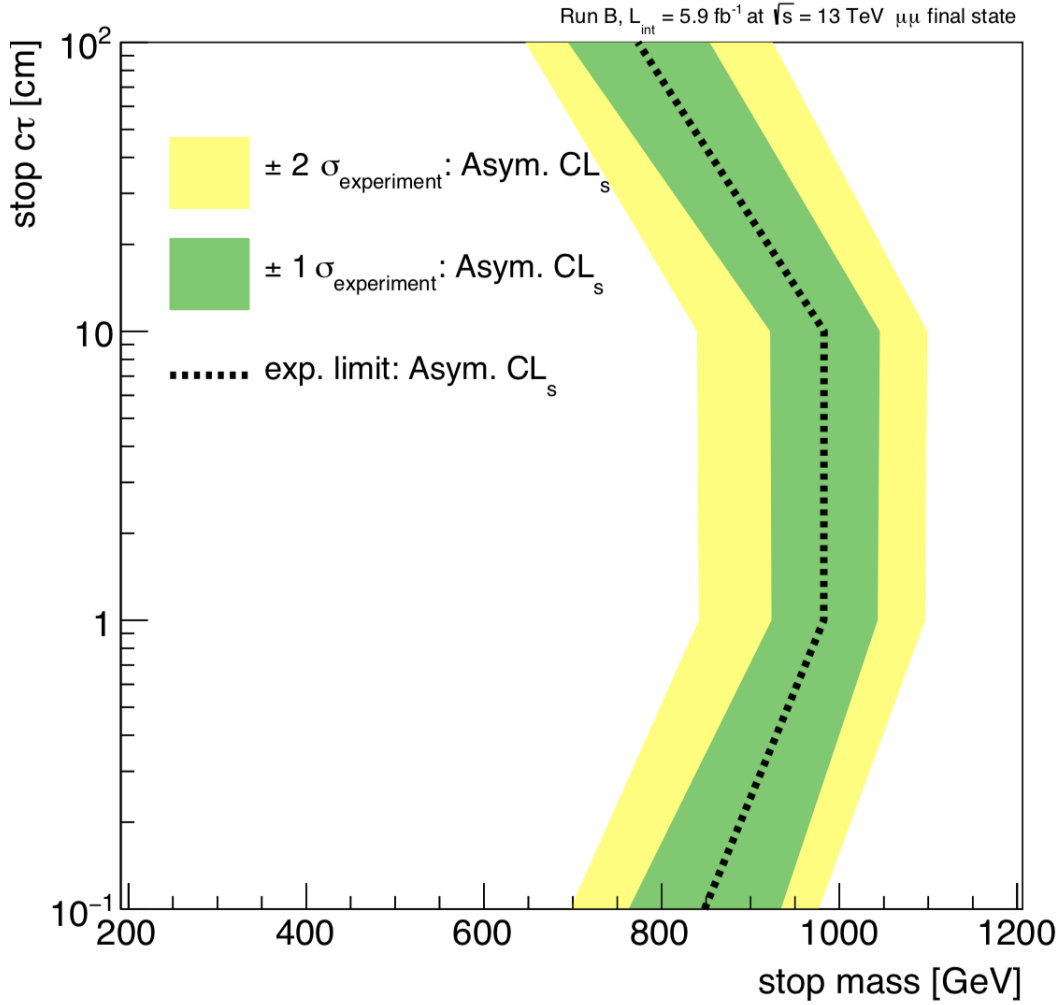


Figure 21: Expected limit for the production cross section for a pair of stops at 13 TeV center-of-mass energy with corresponding integrated luminosity 5.9 fb^{-1} . The dashed black line represents the exclusion contours for the stop pair. The region on the left side of the limit represents the excluded stops by the analysis, assuming no excess over the background. The green band corresponds to the one σ deviation, while the yellow band two σ . This result is for Run B.

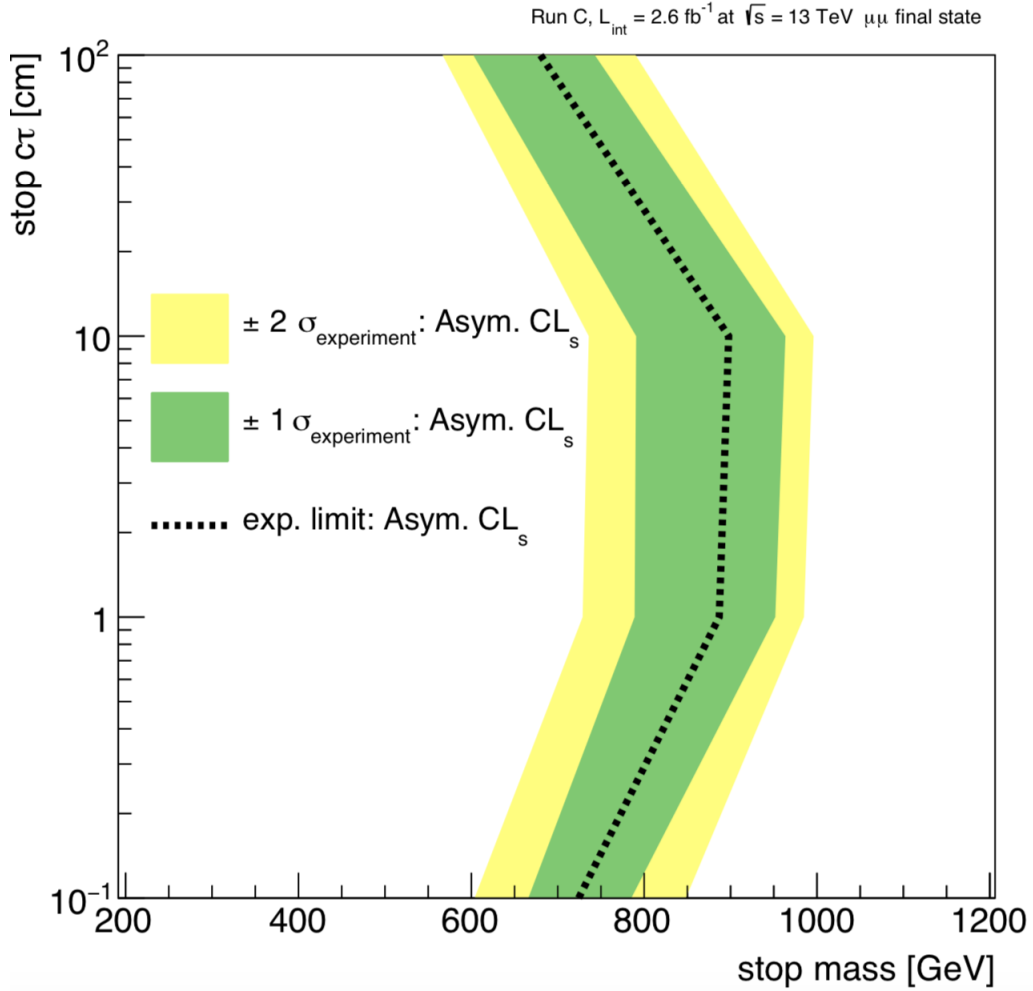


Figure 22: Expected limit for the production cross section for a pair of stops at 13 TeV center-of-mass energy with corresponding integrated luminosity 2.6 fb^{-1} . The dashed black line represents the exclusion contours for the stop pair. The region on the left side of the limit represents the excluded stops by the analysis, assuming no excess over the background. The green band corresponds to the one σ deviation, while the yellow band two σ . This result is for Run C.

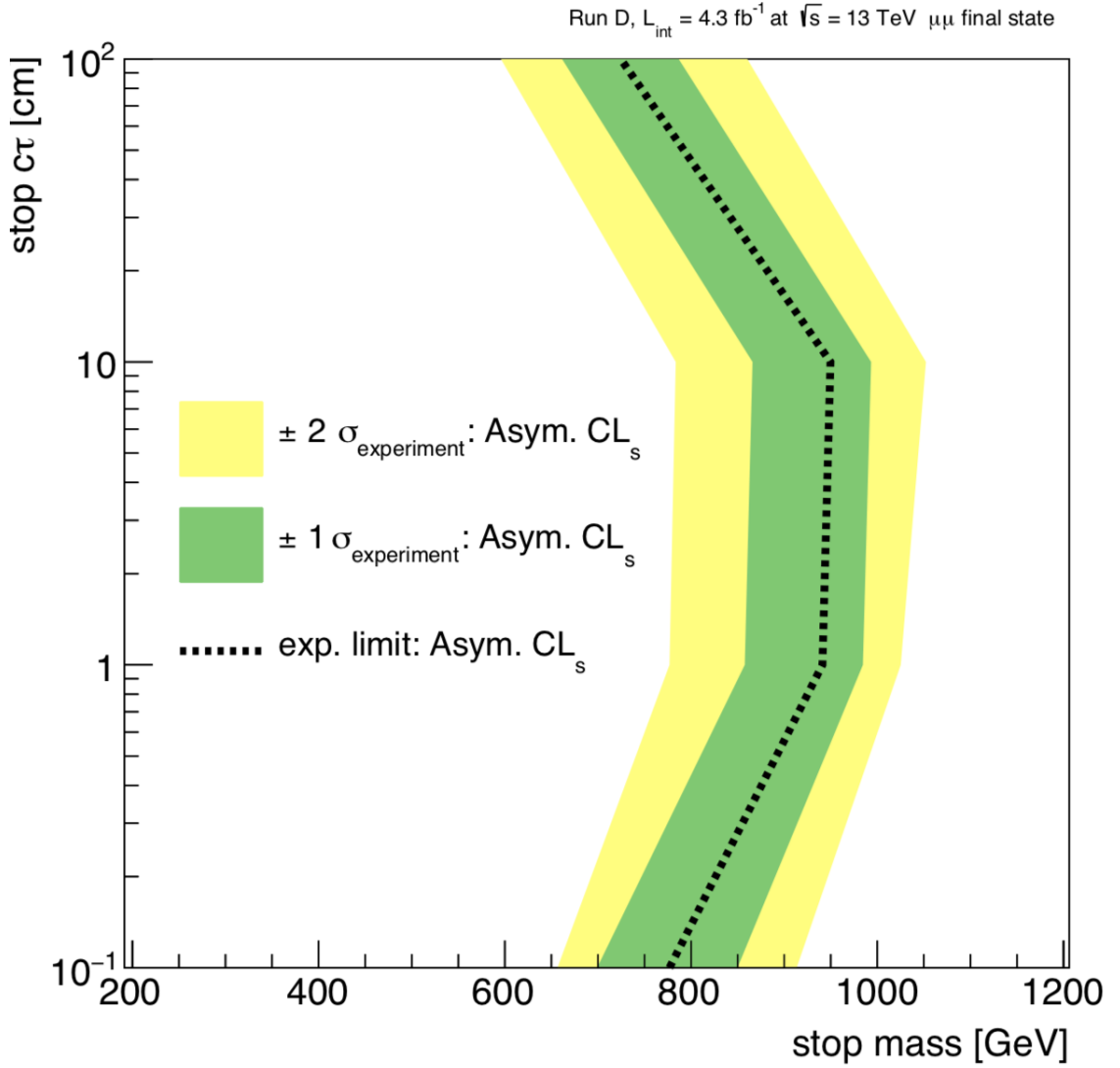


Figure 23: Expected limit for the production cross section for a pair of stops at 13 TeV center-of-mass energy with corresponding integrated luminosity 4.3 fb^{-1} . The dashed black line represents the exclusion contours for the stop pair. The region on the left side of the limit represents the excluded stops by the analysis, assuming no excess over the background. The green band corresponds to the one σ deviation, while the yellow band two σ . This result is for Run D.

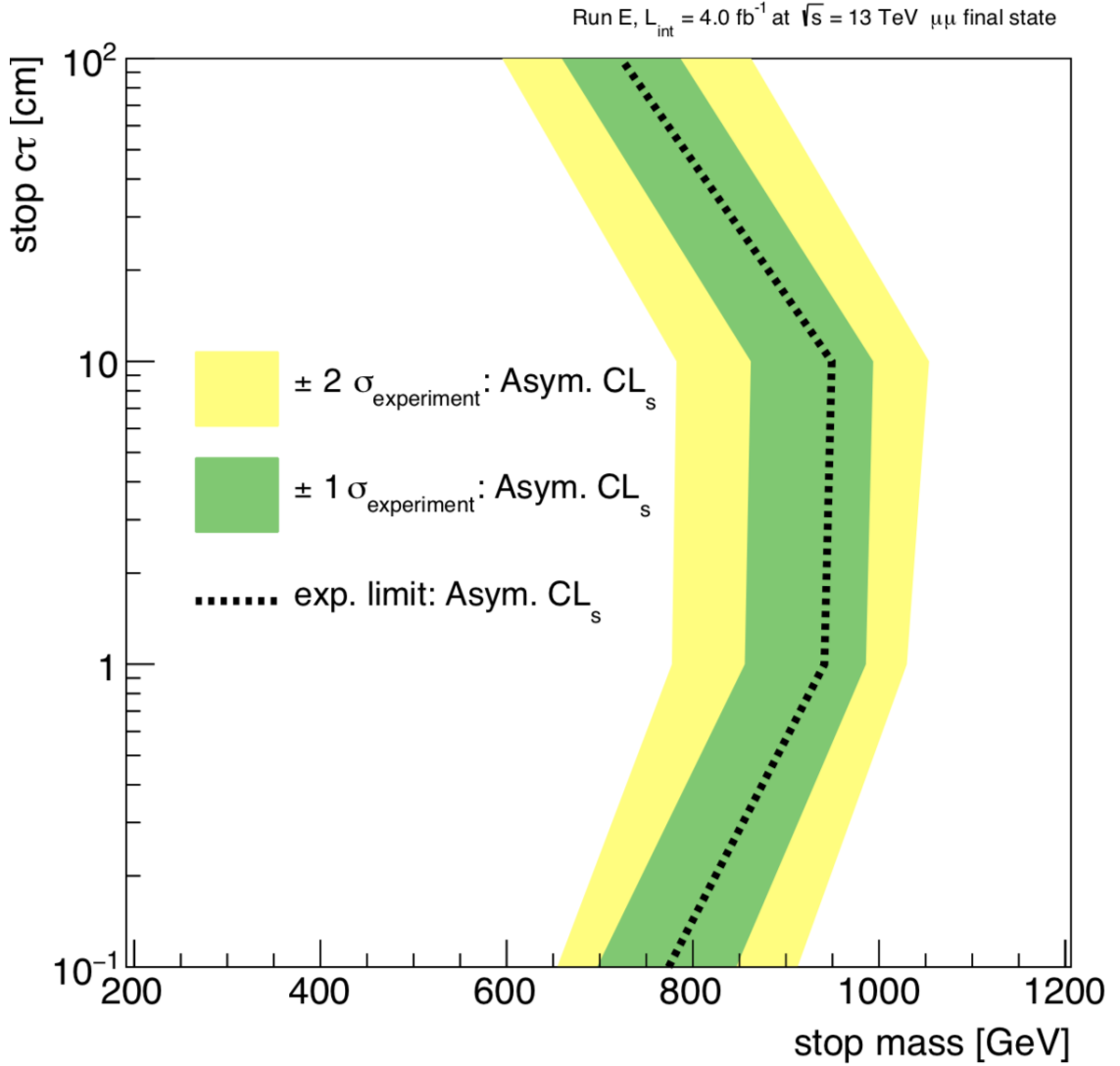


Figure 24: Expected limit for the production cross section for a pair of stops at 13 TeV center-of-mass energy with corresponding integrated luminosity 4.0 fb^{-1} . The dashed black line represents the exclusion contours for the stop pair. The region on the left side of the limit represents the excluded stops by the analysis, assuming no excess over the background. The green band corresponds to the one σ deviation, while the yellow band two σ . This result is for Run E.

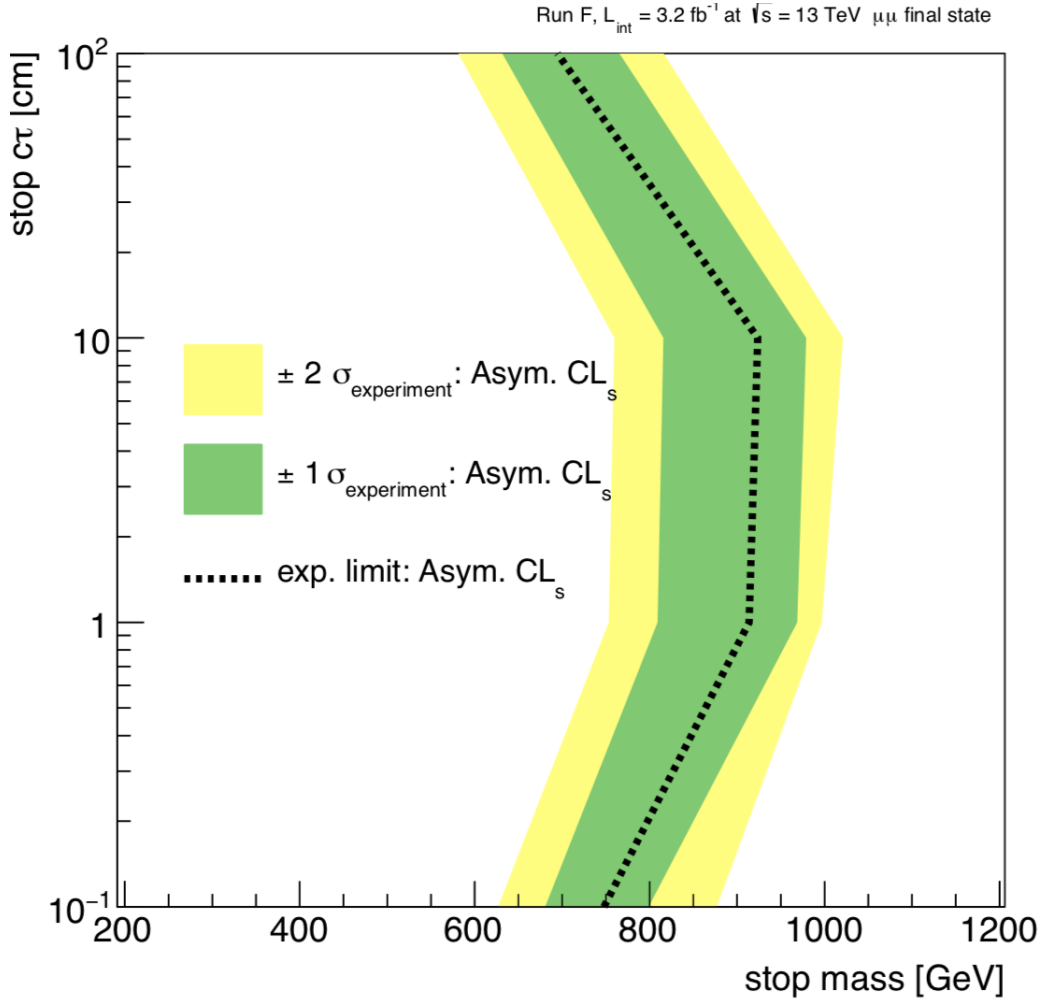


Figure 25: Expected limit for the production cross section for a pair of stops at 13 TeV center-of-mass energy with corresponding integrated luminosity 3.2 fb^{-1} . The dashed black line represents the exclusion contours for the stop pair. The region on the left side of the limit represents the excluded stops by the analysis, assuming no excess over the background. The green band corresponds to the one σ deviation, while the yellow band two σ . This result is for Run F.

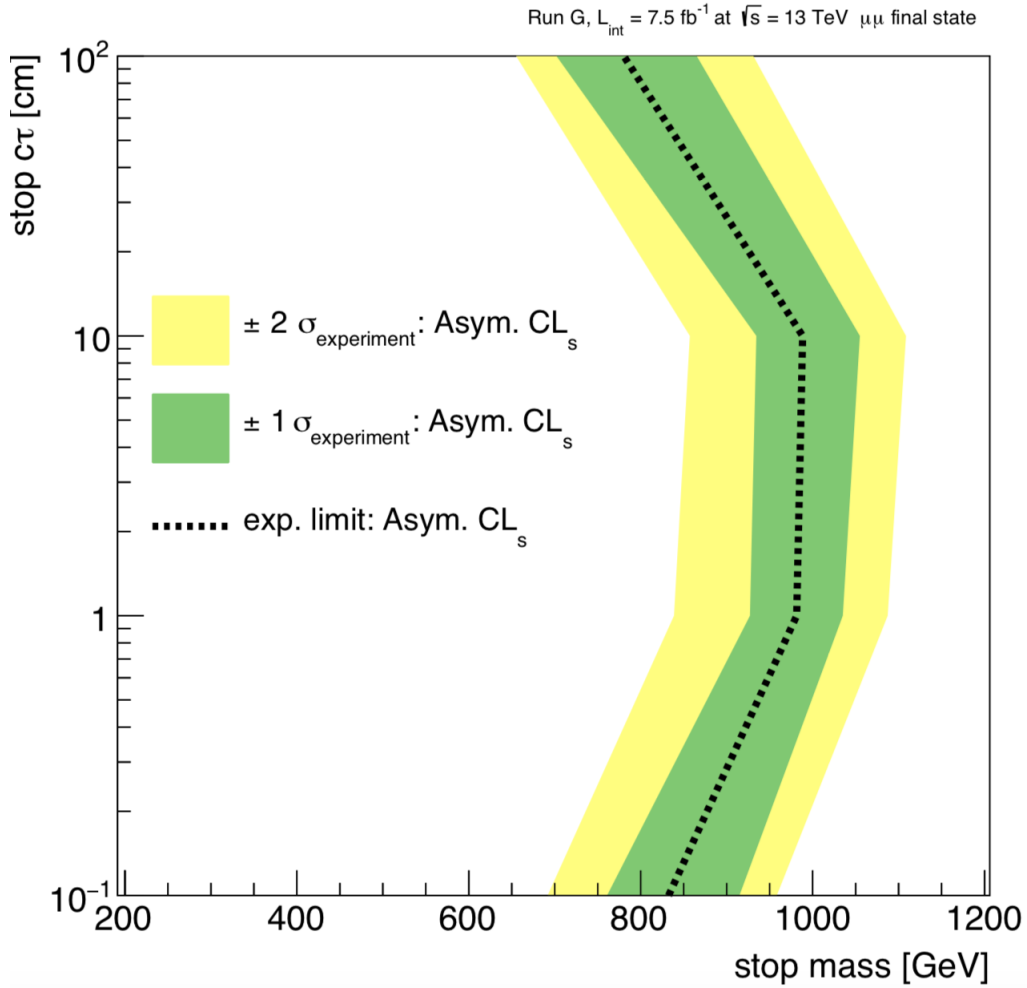


Figure 26: Expected limit for the production cross section for a pair of stops at 13 TeV center-of-mass energy with corresponding integrated luminosity 7.5 fb^{-1} . The dashed black line represents the exclusion contours for the stop pair. The region on the left side of the limit represents the excluded stops by the analysis, assuming no excess over the background. The green band corresponds to the one σ deviation, while the yellow band two σ . This result is for Run G.

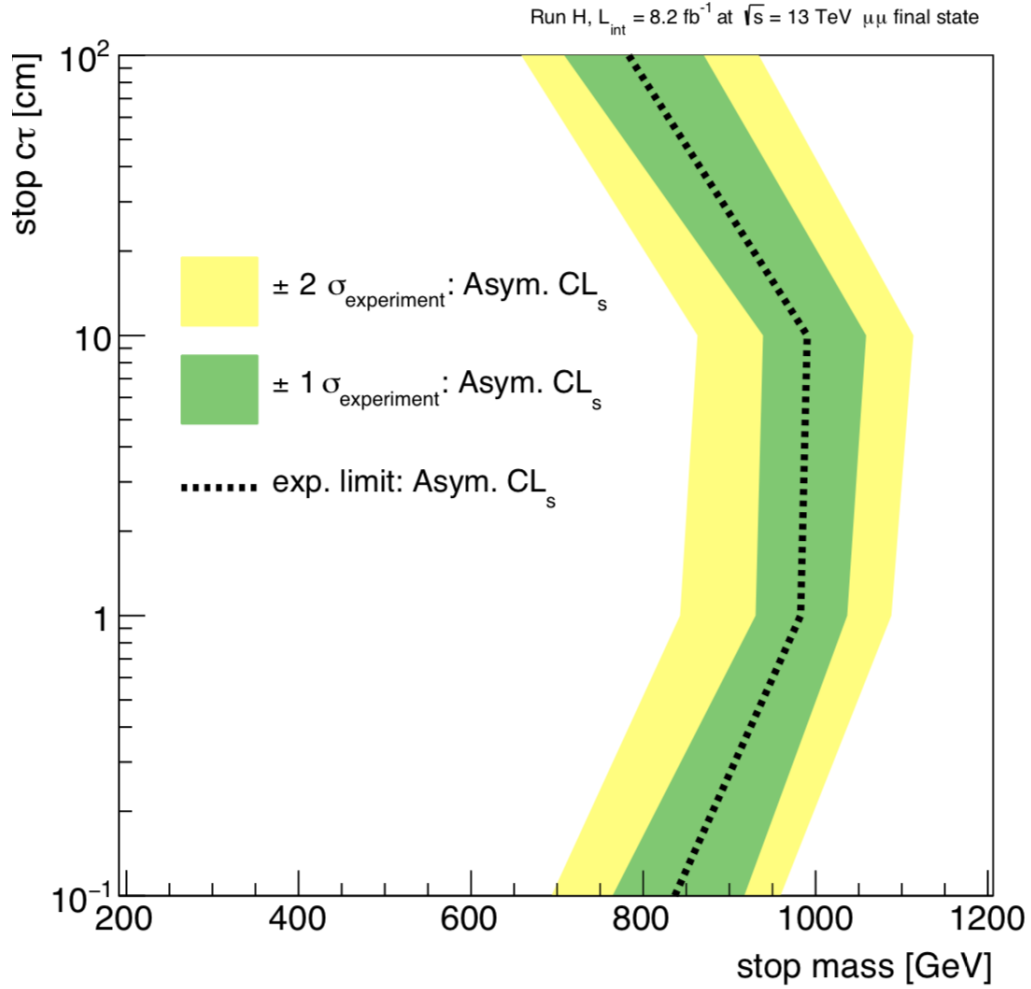


Figure 27: Expected limit for the production cross section for a pair of stops at 13 TeV center-of-mass energy with corresponding integrated luminosity 8.2 fb^{-1} . The dashed black line represents the exclusion contours for the stop pair. The region on the left side of the limit represents the excluded stops by the analysis, assuming no excess over the background. The green band corresponds to the one σ deviation, while the yellow band two σ . This result is for Run H.

12 Comparison to Official CMS Results

There are in fact previous searches, where the same analysis was performed for older data-sets taken by the CMS detector. The latest published results for a search for new long-lived particles decaying to leptons were presented using proton-proton collisions produced by the LHC at a center-of-mass energy of 8 TeV are presented here [13]. The corresponding luminosity was 19.7 fb^{-1} . Figure 28 shows the limit plot obtained from this last search. Notice the full black line, which represents the observed limit by unblinding the data. The results for the limit obtained for the same topology assumed in

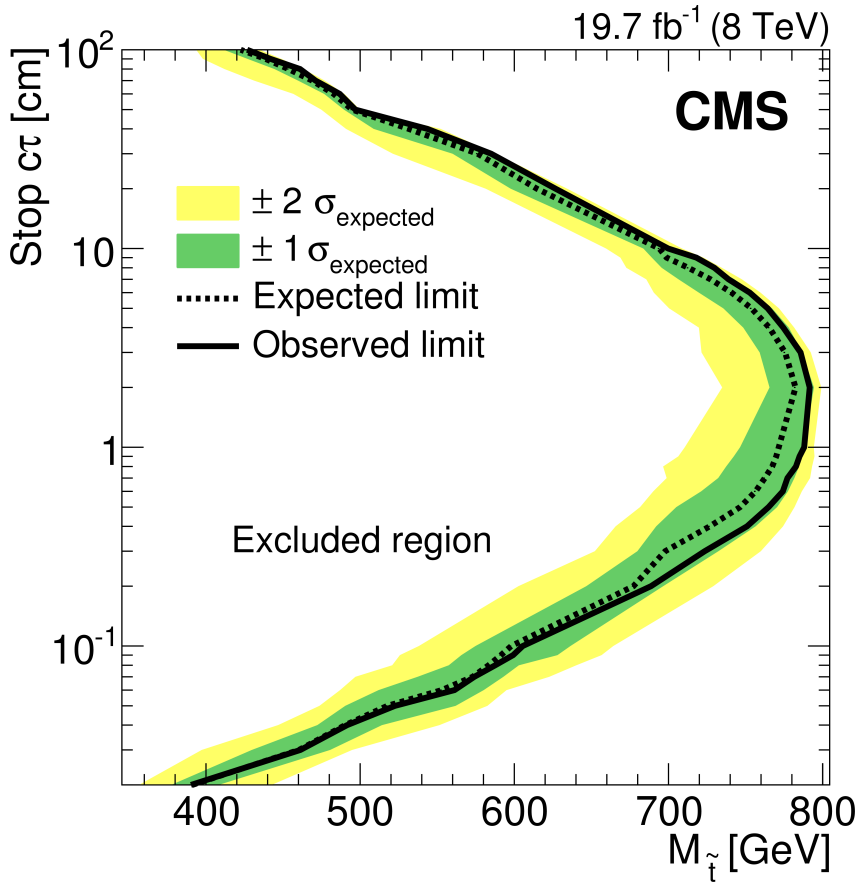


Figure 28: Expected and observed 95% CL cross section exclusion contours for top squark pair production at a center-of-mass energy of 8 TeV from the CMS analysis [13], with corresponding luminosity of 19.7 fb^{-1} .

this thesis, showed the exclusion of masses up to 790 GeV at 95% confidence level. However the final state is slightly different from the one used in this thesis, one expected one electron and one muon instead of two muons in the

final state. In this case there are differences in the background, where for example the Drell-Yan background is significantly lower than in the $\mu\mu$ case. Also the branching ratio for $e\mu$ -events is approximately twice as big as the one for $\mu\mu$ ($e\mu$ and μe case together). This would mean that for exactly the same integrated luminosity one would expect the $\mu\mu$ case to be less performant than the $e\mu$ case because of the difference in background contributions.

Comparing this result to the obtained limit plots in this thesis, it is clear that the older limits are lower. This is because of the higher center-of-mass energy in the 2016 CMS data, where the cross sections for the stops production have increased. Taking the Run with lowest luminosity, the limit obtained from Run C are still higher, excluding masses up to 900 GeV at 95%. The highest limit is obtained from Run H, where stops with 1000 GeV and $c\tau = 10$ and 100 are excluded.

There is also a preliminary search performed with the 2015 CMS data [14]. The results are presented for an integrated luminosity of 2.6 fb^{-1} at 13 TeV. Figure 29 shows the limit plot obtained for this analysis.

This result is also for a $e\mu$ final state, where stop quarks with masses up to 870 GeV are excluded at 95% confidence level. This result is clearly better than the published one due to the higher cross section at a higher center-of-mass energy. However the integrated luminosity is considerably smaller. Compared to the thesis limit plots, the result is close to Runs with a smaller luminosity, such as Run C.

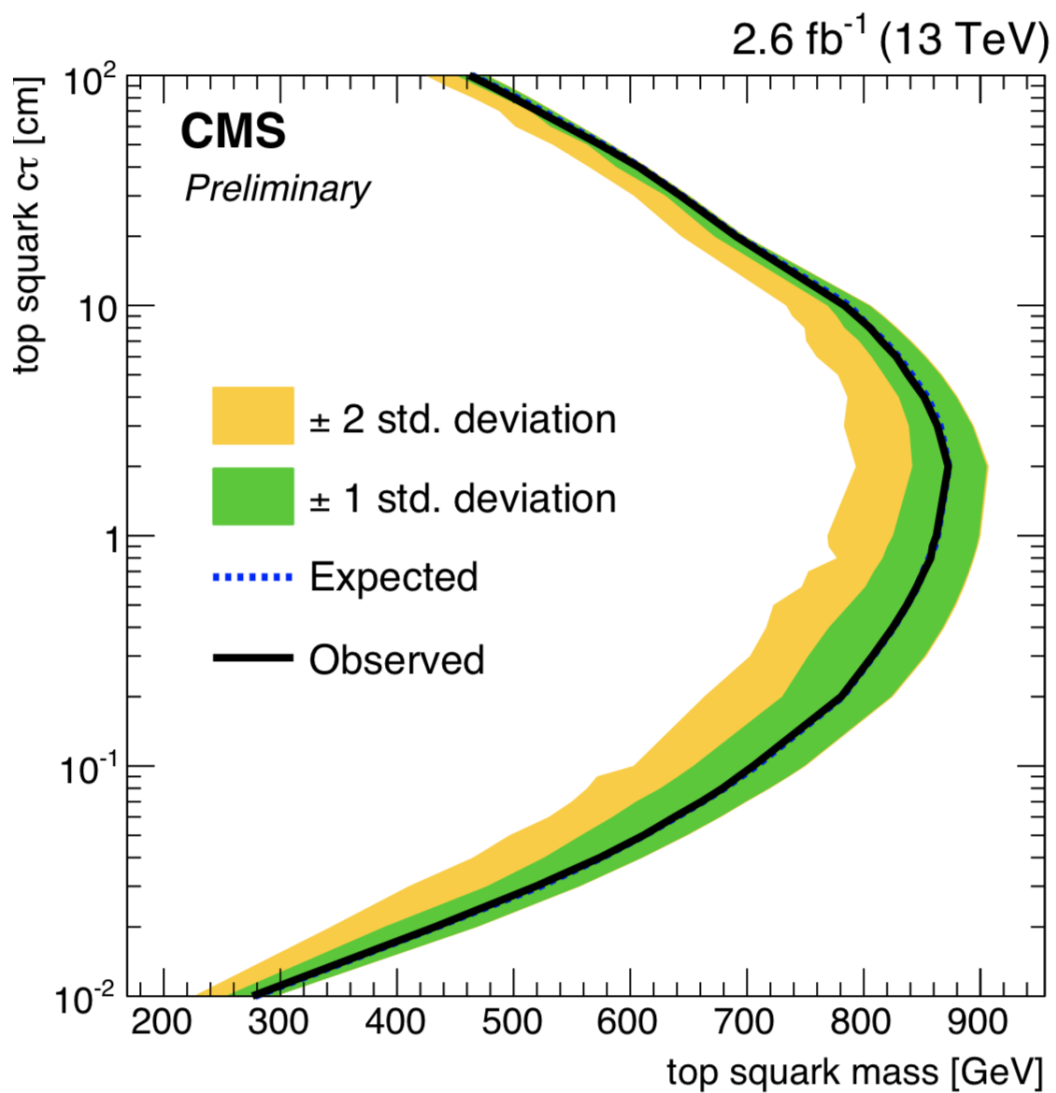


Figure 29: Expected and observed 95% CL cross section exclusion contours for top squark pair production at a center-of-mass energy of 13 TeV from the CMS analysis [14], with corresponding luminosity of 2.6 fb⁻¹.

13 Conclusion

13.1 Non-QCD background estimation

Clearly from the title of this thesis, the major goal of this analysis was to obtain the background contribution in the SRs where new physics signals can appear with a minimal background contamination. After definition of the regions of interest, the background contribution was divided in two groups, depending on their estimation approach; QCD and non-QCD background.

Before starting the estimation with simulated non-QCD MC samples, there were first several corrections needed in order to model the MC to the data correctly. Therefore the Prompt Control Region was defined to obtain the MC-data agreement, which was the guarantee that non-QCD MC is reliable to predict event numbers in other regions. The results were successful and are given in Chapter 7. One could then use the non-QCD MC to predict number of events in the SRs.

13.2 QCD background estimation

The QCD background was approached differently, due to the difficulty in simulation of QCD events. Therefore a data-driven method was used to estimate the number of QCD events in the SRs. This was done by assuming that muons coming from QCD events have a similar d_0 -spectrum. Defining the QCD enriched region, the so called $b\bar{b}$ Control Region, a reasonable number of QCD muons were collected to calculate the transfer factors in the d_0 -spectrum. Using these transfer factors, one could estimate number of event in intermediate regions in the d_0 -spectrum, using Equation 16.

Before estimating the QCD number of events in the SRs, a closure test has been performed in order to prove the reliability of the data-driven method. This last one was successful and validated the method within the one sigma.

13.3 Results

At this point, the background contribution was ready to be estimated. The results for QCD background are given in Table 7 and 8, while the non-QCD background in Table 9. The results obtained showed that the background contribution is as expected relatively low, which confirms the importance of the SRs for a clean signal observation. It was also clear that the QCD estimation had higher uncertainties. This was due to the propagation of un-

certainties from the transfer factors, used for each QCD muon in Equation 17. In addition, the estimations for the 7 different Runs were almost consistent, with the exception that Run G and H behave differently for the QCD estimation. These last Runs had smaller transfer factors, but the larger number of events in the Displaced Control Region compensated in Equation 17, which resulted in a smaller difference in QCD number of events contribution, compared to the other Runs.

13.4 Limits

Having reached the aimed goal, one could check the previously discussed SUSY model in Chapter 2.3.1. For this model a set of samples were available predicting a stop pair production in proton-proton collisions at 13 TeV center-of-mass energy, with different masses and lifetimes. The MC samples has been normalized and corrected on the same way as the non-QCD background samples. Consequently, the expected number of events in the SRs was derived. The results obtained for Run D are listed in Table 11. The low mass samples predicted large numbers, and as the mass become larger, the number of events became smaller. This was the manifestation of the corresponding cross section at 13 TeV, which is expected to drop as the mass becomes larger. For the lifetime, samples with $c\tau = 10$ and 100 mm had the highest number of events in the SRs, while $c\tau = 1$ dominant in the low d_0 -region (PCR and DCR) and $c\tau = 1000$ mm dominant beyond the $d_0 = 2$ cm, which is the upper limit of the SRs.

Assuming the expected background in the SRs, limits has been set for the production cross section of the stops in proton-proton collisions at 13 TeV with a $\mu\mu$ final state. The limit plots are shown in Figures 21 - 27, where the upper limit is given by the black dashed line. Comparing the limits from all Runs, it is clear that stops with a mass lower or equal to 900 GeV are excluded. The highest limit is obtained from Run H, where stops with 1000 GeV and $c\tau = 10$ and 100 are excluded.

Comparing this result to the published limits in 2014 [13], it is clear that the older limits are lower. This is because of the higher center-of-mass energy in 2016 CMS data, where the referred analysis was at 8 TeV corresponding to an integrated luminosity of 19.7 fb^{-1} . Compared to the limit plot for the preliminary analysis at 13 TeV, Figure 29, the result is close to Runs with a smaller luminosity, such as Run C.

14 Outlook

However, there are certainly a few things that can be improved in the analysis. After the performance of a closure test to prove the reliability of the data-driven method for the QCD estimation, one can also prove the reliability of the transfer factors, by performing a closure test where a completely independent QCD regions can be used to estimate the QCD background with the transfer factors listed in Figure 16. This would prove that muons from QCD do really behave similarly or not. Another weakness of this analysis is the fact that the limits can be considerably improved, if all the previously shown limits for all Runs are combined. This combined limit is believed to achieve the exclusion of stops with a mass up to 1200 GeV.

15 Summary

In this thesis, the background contribution has been estimated for searches for new physics in dimuon final states, occurring in proton-proton collisions at 13 TeV center-of-mass energy. The 2016 data of the CMS detector has been used for this analysis, with a corresponding integrated luminosity of 35.7 fb^{-1} . The background estimation is determined separately for respectively QCD and non-QCD background. For the QCD background, which cannot be estimated with Monte Carlo simulations, a data-driven method is used to predict the number of events in the signal regions. The signal regions were chosen to have a low background contribution, which is optimal for signal estimation with a minimal background contamination. This involved detailed studies and understanding of properties of misidentification of muons that mimic the signal. A new physics model based on Displaced Supersymmetry was used for hypothesis testing. This model predicts pair production of supersymmetric top quarks. For this topology the number of expected events were predicted for different masses and lifetimes of the supersymmetric top quarks. Finally limits were set to estimate the sensitivity for an analysis using the 2016 CMS data-set. An analysis using this method on that data-set is expected to exclude stop quarks with masses up to 1000 GeV at 95% confidence level. The results were compared to limits obtained in published CMS results. The limits obtained in this thesis showed the potential to significantly improve on the existing results using the 2016 data.

References

- [1] Yndurin, F.J. (1996). Relativistic Quantum Mechanics and Introduction to Field Theory (1st ed.). Springer. ISBN 978-3-540-60453-2.
- [2] ATLAS; CMS (26 March 2015). "Combined Measurement of the Higgs Boson Mass in pp Collisions at s=7 and 8 TeV with the ATLAS and CMS Experiments". Physical Review Letters.
- [3] I.J.R. Aitchison, Supersymmetry and the MSSM: An Elementary Introduction, 2005, arXiv:hep-ph/0505105
- [4] Cumulative integrated luminosity recorded by CMS in 2016 <https://twiki.cern.ch/twiki/bin/view/CMSPublic/LumiPublicResults>
- [5] "CMS Collaboration - CMS Experiment". cms.web.cern.ch. Retrieved 20 December 2017
- [6] CMS Collaboration, *Search for displaced Supersymmetry in events with two leptons with large impact parameters with the CMS detector at the LHC*, 2015.
- [7] T. Sjostrand, S. Mrenna, and P. Z. Skands, PYTHIA 6.4 Physics and Manual, JHEP 05 (2006) 026, doi:10.1088/1126-6708/2006/05/026, arXiv:hep-ph/0603175.
- [8] J. Alwall et al., MadGraph 5 : Going Beyond, JHEP 06 (2011) 128, doi:10.1007/JHEP06(2011)128, arXiv:1106.0522.
- [9] S. Alioli, P. Nason, C. Oleari, and E. Re, A general framework for implementing NLO calculations in shower Monte Carlo programs: the POWHEG BOX, JHEP 06 (2010) 043, doi:10.1007/JHEP06(2010)043, arXiv:1002.2581.
- [10] S. Frixione and B. R. Webber, Matching NLO QCD computations and parton shower simulations, JHEP 06 (2002) 029, doi:10.1088/1126-6708/2002/06/029, arXiv:hep-ph/0204244.
- [11] S. Jadach, J. H. Kuhn, and Z. Was, TAUOLA: A Library of Monte Carlo programs to simulate decays of polarized tau leptons, Comput. Phys. Commun. 64 (1990) 275299, doi:10.1016/0010-4655(91)90038-M.
- [12] S. P. et al, SUSY cross sections for CMS at 13 TeV., <https://twiki.cern.ch/twiki/bin/view/LHCPhysics/SUSYCrossSections13TeVstopsbottom>.

- [13] CMS Collaboration, *Search for Displaced Supersymmetry in events with an electron and a muon with large impact parameters*, 2014.
- [14] CMS Collaboration, *Search for displaced leptons in the $e\text{-}\mu$ channel*, 2016.
- [15] CMS Collaboration, *Search for Displaced Supersymmetry in Dilepton Final States at 13 TeV*, 2016.
- [16] CMS Collaboration, *Search for new physics in events with leptons with large impact parameters: parametrisation study*, 2015.
- [17] S. Pandolfi, LHCb observes an exceptionally large group of particles. [Online]. 2017. <https://home.cern/about/updates/2017/03/lhcb-observes-exceptionally-large-group-particles>

Appendix

Table 11: The number of events of the different processes contributing to the background in the Prompt Control Region.

Run	Process	Number of events	Contribution fraction
B	$Z \rightarrow \mu\mu$	$(1.111 \pm 0.004)*10^6$	0.98477 ± 0.00006
	Diboson	2879 ± 9	0.002551 ± 0.000013
	$t\bar{t}$	12071 ± 14	0.01070 ± 0.00004
	Singletop	2163 ± 7	0.001917 ± 0.000010
	$W \rightarrow \mu\nu$	70 ± 15	$(6.2 \pm 1.4)*10^{-5}$
	Data	0.0 ± 0	/
	C	$Z \rightarrow \mu\mu$	$(4.983 \pm 0.019)*10^5$
Diboson		1291 ± 4	0.002551 ± 0.000013
$t\bar{t}$		5413 ± 6	0.01070 ± 0.00004
Singletop		969.9 ± 3.3	0.001917 ± 0.000010
$W \rightarrow \mu\nu$		32 ± 7	$(6.2 \pm 1.4)*10^{-5}$
Data		$(4.386 \pm 0.007)*10^5$	/
D		$Z \rightarrow \mu\mu$	$(8.216 \pm 0.032)*10^5$
	Diboson	2129 ± 7	0.002551 ± 0.000013
	$t\bar{t}$	8925 ± 10	0.01070 ± 0.00004
	Singletop	1599 ± 5	0.001917 ± 0.000010
	$W \rightarrow \mu\nu$	52 ± 11	$(6.2 \pm 1.4)*10^{-5}$
	Data	$(7.226 \pm 0.009)*10^5$	/
	E	$Z \rightarrow \mu\mu$	$(7.638 \pm 0.030)*10^5$
Diboson		1979 ± 7	0.002551 ± 0.000013
$t\bar{t}$		8297 ± 10	0.01070 ± 0.00004
Singletop		1487 ± 5	0.001917 ± 0.000010
$W \rightarrow \mu\nu$		48 ± 10	$(6.2 \pm 1.4)*10^{-5}$
Data		$(6.688 \pm 0.008)*10^5$	/
F		$Z \rightarrow \mu\mu$	$(5.984 \pm 0.023)*10^5$
	Diboson	1550 ± 5	0.002551 ± 0.000013
	$t\bar{t}$	6500 ± 8	0.01070 ± 0.00004
	Singletop	1165 ± 4	0.001917 ± 0.000010
	$W \rightarrow \mu\nu$	38 ± 8	$(6.2 \pm 1.4)*10^{-5}$
	Data	$(5.227 \pm 0.007)*10^5$	/
	G	$Z \rightarrow \mu\mu$	$(1.4598 \pm 0.0005)*10^6$
Diboson		3715 ± 12	0.002507 ± 0.000008
$t\bar{t}$		15557 ± 18	0.010498 ± 0.000013
Singletop		2787 ± 9	0.001881 ± 0.000006
$W \rightarrow \mu\nu$		91 ± 20	$(6.1 \pm 1.3)*10^{-5}$
Data		$(1.3528 \pm 0.0012)*10^6$	/
H		$Z \rightarrow \mu\mu$	$(1.5857 \pm 0.0006)*10^6$
	Diboson	4036 ± 13	0.002507 ± 0.000008
	$t\bar{t}$	16899 ± 20	0.010498 ± 0.000013
	Single top	3027 ± 10	0.001881 ± 0.000006
	$W \rightarrow \mu\nu$	98 ± 21	$(6.1 \pm 1.3)*10^{-5}$
	Data	$(1.5592 \pm 0.0012)*10^6$	/

Table 12: The signal estimation for $\mu\mu$ isolated in the Signal Regions obtained from MC for Run B.

stop t	SR1	SR2	SR3
stop 200 GeV 1000	2708.218 \pm 114.088	2324.166 \pm 105.451	1943.632 \pm 96.769
stop200 GeV 100	18699.942 \pm 302.576	16434.785 \pm 283.994	14188.194 \pm 264.095
stop200GeV10	23593.613 \pm 338.946	16990.341 \pm 287.616	11063.851 \pm 231.866
stop200GeV1	6675.878 \pm 179.167	1689.873 \pm 90.209	319.367 \pm 38.989
stop300GeV1000	477.872 \pm 17.576	415.748 \pm 16.398	355.736 \pm 15.151
stop300GeV100	3200.777 \pm 45.169	2795.506 \pm 42.203	2413.083 \pm 39.211
stop300GeV10	3627.681 \pm 48.084	2620.862 \pm 40.851	1699.604 \pm 32.871
stop300GeV1	1124.414 \pm 26.947	301.907 \pm 13.942	63.619 \pm 6.447
stop400GeV1000	123.579 \pm 4.118	106.466 \pm 3.824	91.452 \pm 3.549
stop400GeV100	757.574 \pm 10.282	670.777 \pm 9.681	576.05 \pm 8.973
stop400GeV10	848.737 \pm 10.804	614.996 \pm 9.205	405.281 \pm 7.478
stop400GeV1	258.983 \pm 5.979	69.951 \pm 3.113	15.708 \pm 1.481
stop500GeV1000	41.554 \pm 1.271	36.199 \pm 1.188	31.277 \pm 1.105
stop500GeV100	226.262 \pm 2.976	198.777 \pm 2.79	169.89 \pm 2.579
stop500GeV10	250.849 \pm 3.149	180.601 \pm 2.671	116.904 \pm 2.15
stop500GeV1	76.551 \pm 1.721	18.359 \pm 0.842	4.026 \pm 0.396
stop600GeV1000	14.853 \pm 0.442	12.417 \pm 0.405	10.949 \pm 0.381
stop600GeV100	78.715 \pm 1.016	69.793 \pm 0.957	60.05 \pm 0.888
stop600GeV10	84.962 \pm 1.055	60.601 \pm 0.891	38.924 \pm 0.715
stop600GeV1	25.459 \pm 0.577	6.186 \pm 0.285	1.018 \pm 0.117
stop700GeV1000	6.075 \pm 0.175	5.263 \pm 0.163	4.523 \pm 0.151
stop700GeV100	29.565 \pm 0.386	26.26 \pm 0.364	22.451 \pm 0.337
stop700GeV10	31.673 \pm 0.399	22.745 \pm 0.338	14.596 \pm 0.271
stop700GeV1	9.52 \pm 0.219	2.463 \pm 0.112	0.405 \pm 0.046
stop800GeV1000	2.655 \pm 0.075	2.294 \pm 0.07	1.952 \pm 0.065
stop800GeV100	12.842 \pm 0.166	11.482 \pm 0.157	9.887 \pm 0.145
stop800GeV10	13.59 \pm 0.17	9.661 \pm 0.144	6.023 \pm 0.114
stop800GeV1	4.138 \pm 0.094	0.998 \pm 0.046	0.2 \pm 0.021
stop1000GeV1000	0.58 \pm 0.016	0.507 \pm 0.015	0.439 \pm 0.014
stop1000GeV100	2.715 \pm 0.035	2.412 \pm 0.033	2.08 \pm 0.031
stop1000GeV10	2.822 \pm 0.036	1.998 \pm 0.03	1.282 \pm 0.024
stop1000GeV1	0.851 \pm 0.02	0.206 \pm 0.01	0.036 \pm 0.004
stop1100GeV1000	0.293 \pm 0.008	0.253 \pm 0.008	0.218 \pm 0.007
stop1100GeV100	1.335 \pm 0.018	1.185 \pm 0.017	1.007 \pm 0.015
stop1100GeV10	1.391 \pm 0.018	0.976 \pm 0.015	0.605 \pm 0.012
stop1100GeV1	0.405 \pm 0.01	0.101 \pm 0.005	0.017 \pm 0.002
stop1200GeV1000	0.163 \pm 0.004	0.141 \pm 0.004	0.124 \pm 0.004
stop1200GeV100	0.708 \pm 0.009	0.63 \pm 0.009	0.546 \pm 0.008
stop1200GeV10	0.712 \pm 0.009	0.496 \pm 0.008	0.307 \pm 0.006
stop1200GeV1	0.207 \pm 0.005	0.05 \pm 0.002	0.01 \pm 0.001

Table 13: The signal estimation for $\mu\mu$ isolated in the Signal Regions obtained from MC for Run C.

stop t	SR1	SR2	SR3
stop200GeV1000	1214.41 \pm 51.159	1042.195 \pm 47.286	871.557 \pm 43.393
stop200GeV100	8385.367 \pm 135.68	7369.632 \pm 127.348	6362.223 \pm 118.425
stop200GeV10	10579.771 \pm 151.989	7618.753 \pm 128.972	4961.216 \pm 103.972
stop200GeV1	2993.575 \pm 80.341	757.767 \pm 40.451	143.21 \pm 17.483
stop300GeV1000	214.286 \pm 7.881	186.429 \pm 7.353	159.518 \pm 6.794
stop300GeV100	1435.282 \pm 20.255	1253.552 \pm 18.925	1082.067 \pm 17.583
stop300GeV10	1626.713 \pm 21.562	1175.238 \pm 18.318	762.131 \pm 14.74
stop300GeV1	504.206 \pm 12.083	135.38 \pm 6.252	28.528 \pm 2.891
stop400GeV1000	55.415 \pm 1.847	47.741 \pm 1.715	41.008 \pm 1.591
stop400GeV100	339.709 \pm 4.611	300.787 \pm 4.341	258.31 \pm 4.024
stop400GeV10	380.588 \pm 4.845	275.774 \pm 4.128	181.735 \pm 3.353
stop400GeV1	116.132 \pm 2.681	31.367 \pm 1.396	7.044 \pm 0.664
stop500GeV1000	18.633 \pm 0.57	16.232 \pm 0.533	14.025 \pm 0.495
stop500GeV100	101.46 \pm 1.335	89.135 \pm 1.251	76.181 \pm 1.157
stop500GeV10	112.485 \pm 1.412	80.984 \pm 1.198	52.422 \pm 0.964
stop500GeV1	34.327 \pm 0.772	8.232 \pm 0.377	1.805 \pm 0.178
stop600GeV1000	6.66 \pm 0.198	5.568 \pm 0.182	4.91 \pm 0.171
stop600GeV100	35.297 \pm 0.456	31.296 \pm 0.429	26.927 \pm 0.398
stop600GeV10	38.098 \pm 0.473	27.175 \pm 0.4	17.454 \pm 0.321
stop600GeV1	11.416 \pm 0.259	2.774 \pm 0.128	0.457 \pm 0.052
stop700GeV1000	2.724 \pm 0.078	2.36 \pm 0.073	2.028 \pm 0.068
stop700GeV100	13.257 \pm 0.173	11.776 \pm 0.163	10.068 \pm 0.151
stop700GeV10	14.203 \pm 0.179	10.199 \pm 0.152	6.545 \pm 0.121
stop700GeV1	4.269 \pm 0.098	1.104 \pm 0.05	0.182 \pm 0.02
stop800GeV1000	1.191 \pm 0.034	1.029 \pm 0.031	0.876 \pm 0.029
stop800GeV100	5.758 \pm 0.074	5.149 \pm 0.07	4.433 \pm 0.065
stop800GeV10	6.094 \pm 0.076	4.332 \pm 0.064	2.701 \pm 0.051
stop800GeV1	1.855 \pm 0.042	0.448 \pm 0.021	0.09 \pm 0.009
stop1000GeV1000	0.26 \pm 0.007	0.227 \pm 0.007	0.197 \pm 0.006
stop1000GeV100	1.218 \pm 0.016	1.082 \pm 0.015	0.933 \pm 0.014
stop1000GeV10	1.266 \pm 0.016	0.896 \pm 0.014	0.575 \pm 0.011
stop1000GeV1	0.381 \pm 0.009	0.092 \pm 0.004	0.016 \pm 0.002
stop1100GeV1000	0.131 \pm 0.004	0.113 \pm 0.003	0.098 \pm 0.003
stop1100GeV100	0.599 \pm 0.008	0.531 \pm 0.007	0.452 \pm 0.007
stop1100GeV10	0.624 \pm 0.008	0.437 \pm 0.007	0.272 \pm 0.005
stop1100GeV1	0.182 \pm 0.004	0.046 \pm 0.002	0.007 \pm 0.001
stop1200GeV1000	0.073 \pm 0.002	0.063 \pm 0.002	0.056 \pm 0.002
stop1200GeV100	0.317 \pm 0.004	0.283 \pm 0.004	0.245 \pm 0.004
stop1200GeV10	0.319 \pm 0.004	0.222 \pm 0.003	0.138 \pm 0.003
stop1200GeV1	0.093 \pm 0.002	0.022 \pm 0.001	0.004 \pm 0.0

Table 14: The signal estimation for $\mu\mu$ isolated in the Signal Regions obtained from MC for Run E.

stop t	SR1	SR2	SR3
stop200GeV1000	1861.541 \pm 78.42	1597.556 \pm 72.483	1335.989 \pm 66.516
stop200GeV100	12853.731 \pm 207.981	11296.736 \pm 195.209	9752.502 \pm 181.53
stop200GeV10	16217.481 \pm 232.98	11678.607 \pm 197.698	7604.931 \pm 159.377
stop200GeV1	4588.781 \pm 123.154	1161.563 \pm 62.007	219.522 \pm 26.799
stop300GeV1000	328.474 \pm 12.081	285.772 \pm 11.272	244.521 \pm 10.414
stop300GeV100	2200.11 \pm 31.048	1921.54 \pm 29.009	1658.675 \pm 26.952
stop300GeV10	2493.55 \pm 33.051	1801.495 \pm 28.08	1168.253 \pm 22.595
stop300GeV1	772.886 \pm 18.522	207.521 \pm 9.584	43.729 \pm 4.432
stop400GeV1000	84.944 \pm 2.831	73.181 \pm 2.628	62.861 \pm 2.439
stop400GeV100	520.732 \pm 7.068	461.07 \pm 6.654	395.958 \pm 6.168
stop400GeV10	583.394 \pm 7.426	422.728 \pm 6.327	278.577 \pm 5.14
stop400GeV1	178.016 \pm 4.11	48.082 \pm 2.14	10.797 \pm 1.018
stop500GeV1000	28.563 \pm 0.874	24.882 \pm 0.817	21.498 \pm 0.76
stop500GeV100	155.525 \pm 2.046	136.633 \pm 1.917	116.777 \pm 1.773
stop500GeV10	172.425 \pm 2.165	124.139 \pm 1.836	80.356 \pm 1.478
stop500GeV1	52.619 \pm 1.183	12.619 \pm 0.579	2.767 \pm 0.272
stop600GeV1000	10.21 \pm 0.304	8.535 \pm 0.278	7.526 \pm 0.262
stop600GeV100	54.106 \pm 0.698	47.974 \pm 0.658	41.276 \pm 0.61
stop600GeV10	58.4 \pm 0.726	41.655 \pm 0.612	26.755 \pm 0.491
stop600GeV1	17.5 \pm 0.396	4.252 \pm 0.196	0.7 \pm 0.08
stop700GeV1000	4.176 \pm 0.12	3.618 \pm 0.112	3.109 \pm 0.104
stop700GeV100	20.322 \pm 0.265	18.05 \pm 0.25	15.432 \pm 0.231
stop700GeV10	21.771 \pm 0.274	15.634 \pm 0.232	10.033 \pm 0.186
stop700GeV1	6.544 \pm 0.151	1.693 \pm 0.077	0.279 \pm 0.031
stop800GeV1000	1.825 \pm 0.052	1.577 \pm 0.048	1.342 \pm 0.044
stop800GeV100	8.827 \pm 0.114	7.892 \pm 0.108	6.796 \pm 0.1
stop800GeV10	9.341 \pm 0.117	6.64 \pm 0.099	4.14 \pm 0.078
stop800GeV1	2.844 \pm 0.064	0.686 \pm 0.032	0.138 \pm 0.014
stop1000GeV1000	0.399 \pm 0.011	0.348 \pm 0.011	0.302 \pm 0.01
stop1000GeV100	1.866 \pm 0.024	1.658 \pm 0.023	1.43 \pm 0.021
stop1000GeV10	1.94 \pm 0.025	1.374 \pm 0.021	0.881 \pm 0.017
stop1000GeV1	0.585 \pm 0.014	0.141 \pm 0.007	0.025 \pm 0.003
stop1100GeV1000	0.201 \pm 0.006	0.174 \pm 0.005	0.15 \pm 0.005
stop1100GeV100	0.918 \pm 0.012	0.814 \pm 0.011	0.692 \pm 0.011
stop1100GeV10	0.956 \pm 0.012	0.671 \pm 0.01	0.416 \pm 0.008
stop1100GeV1	0.279 \pm 0.007	0.07 \pm 0.003	0.011 \pm 0.001
stop1200GeV1000	0.112 \pm 0.003	0.097 \pm 0.003	0.085 \pm 0.003
stop1200GeV100	0.487 \pm 0.006	0.433 \pm 0.006	0.375 \pm 0.006
stop1200GeV10	0.489 \pm 0.006	0.341 \pm 0.005	0.211 \pm 0.004
stop1200GeV1	0.142 \pm 0.003	0.034 \pm 0.002	0.007 \pm 0.001

Table 15: The signal estimation for $\mu\mu$ isolated in the Signal Regions obtained from MC for Run F.

stop t	SR1	SR2	SR3
stop200GeV1000	1458.246 \pm 61.431	1251.452 \pm 56.78	1046.553 \pm 52.105
stop200GeV100	10069.028 \pm 162.923	8849.349 \pm 152.918	7639.667 \pm 142.203
stop200GeV10	12704.037 \pm 182.506	9148.49 \pm 154.868	5957.357 \pm 124.849
stop200GeV1	3594.642 \pm 96.473	909.916 \pm 48.573	171.964 \pm 20.994
stop300GeV1000	257.311 \pm 9.464	223.861 \pm 8.83	191.547 \pm 8.158
stop300GeV100	1723.466 \pm 24.321	1505.247 \pm 22.725	1299.33 \pm 21.113
stop300GeV10	1953.333 \pm 25.891	1411.209 \pm 21.997	915.156 \pm 17.7
stop300GeV1	605.444 \pm 14.51	162.563 \pm 7.507	34.256 \pm 3.472
stop400GeV1000	66.541 \pm 2.217	57.327 \pm 2.059	49.242 \pm 1.911
stop400GeV100	407.918 \pm 5.536	361.181 \pm 5.213	310.175 \pm 4.832
stop400GeV10	457.004 \pm 5.817	331.146 \pm 4.957	218.224 \pm 4.027
stop400GeV1	139.45 \pm 3.219	37.665 \pm 1.676	8.458 \pm 0.798
stop500GeV1000	22.375 \pm 0.684	19.492 \pm 0.64	16.841 \pm 0.595
stop500GeV100	121.831 \pm 1.602	107.032 \pm 1.502	91.478 \pm 1.389
stop500GeV10	135.07 \pm 1.696	97.245 \pm 1.438	62.947 \pm 1.157
stop500GeV1	41.219 \pm 0.927	9.885 \pm 0.453	2.168 \pm 0.213
stop600GeV1000	7.998 \pm 0.238	6.686 \pm 0.218	5.895 \pm 0.205
stop600GeV100	42.384 \pm 0.547	37.58 \pm 0.515	32.334 \pm 0.478
stop600GeV10	45.748 \pm 0.568	32.631 \pm 0.48	20.959 \pm 0.385
stop600GeV1	13.708 \pm 0.311	3.331 \pm 0.153	0.548 \pm 0.063
stop700GeV1000	3.271 \pm 0.094	2.834 \pm 0.088	2.436 \pm 0.081
stop700GeV100	15.919 \pm 0.208	14.14 \pm 0.196	12.089 \pm 0.181
stop700GeV10	17.054 \pm 0.215	12.247 \pm 0.182	7.859 \pm 0.146
stop700GeV1	5.126 \pm 0.118	1.326 \pm 0.06	0.218 \pm 0.025
stop800GeV1000	1.43 \pm 0.041	1.235 \pm 0.038	1.051 \pm 0.035
stop800GeV100	6.915 \pm 0.089	6.183 \pm 0.084	5.323 \pm 0.078
stop800GeV10	7.317 \pm 0.092	5.202 \pm 0.077	3.243 \pm 0.061
stop800GeV1	2.228 \pm 0.05	0.538 \pm 0.025	0.108 \pm 0.011
stop1000GeV1000	0.312 \pm 0.009	0.273 \pm 0.008	0.237 \pm 0.008
stop1000GeV100	1.462 \pm 0.019	1.299 \pm 0.018	1.12 \pm 0.017
stop1000GeV10	1.52 \pm 0.019	1.076 \pm 0.016	0.69 \pm 0.013
stop1000GeV1	0.458 \pm 0.011	0.111 \pm 0.005	0.019 \pm 0.002
stop1100GeV1000	0.158 \pm 0.004	0.136 \pm 0.004	0.118 \pm 0.004
stop1100GeV100	0.719 \pm 0.01	0.638 \pm 0.009	0.542 \pm 0.008
stop1100GeV10	0.749 \pm 0.01	0.525 \pm 0.008	0.326 \pm 0.006
stop1100GeV1	0.218 \pm 0.005	0.055 \pm 0.003	0.009 \pm 0.001
stop1200GeV1000	0.088 \pm 0.002	0.076 \pm 0.002	0.067 \pm 0.002
stop1200GeV100	0.381 \pm 0.005	0.339 \pm 0.005	0.294 \pm 0.004
stop1200GeV10	0.383 \pm 0.005	0.267 \pm 0.004	0.165 \pm 0.003
stop1200GeV1	0.111 \pm 0.003	0.027 \pm 0.001	0.005 \pm 0.001

Table 16: The signal estimation for $\mu\mu$ isolated in the Signal Regions obtained from MC for Run G.

stop t	SR1	SR2	SR3
stop200GeV1000	3482.227 \pm 146.686	2987.545 \pm 135.549	2497.214 \pm 124.336
stop200GeV100	24023.57 \pm 388.696	21110.28 \pm 364.766	18220.397 \pm 339.131
stop200GeV10	30330.307 \pm 435.706	21842.272 \pm 369.741	14223.72 \pm 298.085
stop200GeV1	8584.853 \pm 230.385	2172.472 \pm 115.965	410.426 \pm 50.101
stop300GeV1000	613.882 \pm 22.578	533.983 \pm 21.061	456.769 \pm 19.454
stop300GeV100	4111.131 \pm 58.014	3589.767 \pm 54.192	3097.975 \pm 50.337
stop300GeV10	4660.7 \pm 61.772	3367.272 \pm 52.482	2183.437 \pm 42.226
stop300GeV1	1444.813 \pm 34.622	387.89 \pm 17.912	81.72 \pm 8.281
stop400GeV1000	158.688 \pm 5.288	136.661 \pm 4.908	117.333 \pm 4.553
stop400GeV100	972.576 \pm 13.199	860.942 \pm 12.425	739.248 \pm 11.515
stop400GeV10	1090.006 \pm 13.874	789.68 \pm 11.819	520.401 \pm 9.601
stop400GeV1	332.714 \pm 7.68	89.904 \pm 4.001	20.194 \pm 1.904
stop500GeV1000	53.354 \pm 1.632	46.475 \pm 1.526	40.148 \pm 1.418
stop500GeV100	290.472 \pm 3.82	255.154 \pm 3.581	218.041 \pm 3.31
stop500GeV10	322.184 \pm 4.044	231.947 \pm 3.43	150.134 \pm 2.76
stop500GeV1	98.325 \pm 2.21	23.585 \pm 1.081	5.176 \pm 0.509
stop600GeV1000	19.076 \pm 0.568	15.942 \pm 0.52	14.052 \pm 0.488
stop600GeV100	101.048 \pm 1.304	89.583 \pm 1.229	77.062 \pm 1.139
stop600GeV10	109.121 \pm 1.356	77.828 \pm 1.144	49.986 \pm 0.918
stop600GeV1	32.695 \pm 0.741	7.942 \pm 0.366	1.308 \pm 0.15
stop700GeV1000	7.8 \pm 0.225	6.757 \pm 0.209	5.806 \pm 0.194
stop700GeV100	37.951 \pm 0.496	33.705 \pm 0.467	28.814 \pm 0.432
stop700GeV10	40.657 \pm 0.512	29.198 \pm 0.434	18.733 \pm 0.348
stop700GeV1	12.224 \pm 0.282	3.163 \pm 0.144	0.521 \pm 0.059
stop800GeV1000	3.408 \pm 0.097	2.944 \pm 0.09	2.505 \pm 0.083
stop800GeV100	16.484 \pm 0.213	14.737 \pm 0.201	12.688 \pm 0.187
stop800GeV10	17.447 \pm 0.219	12.401 \pm 0.184	7.731 \pm 0.146
stop800GeV1	5.313 \pm 0.12	1.282 \pm 0.059	0.257 \pm 0.027
stop1000GeV1000	0.745 \pm 0.021	0.65 \pm 0.02	0.563 \pm 0.018
stop1000GeV100	3.484 \pm 0.046	3.095 \pm 0.043	2.669 \pm 0.04
stop1000GeV10	3.622 \pm 0.046	2.564 \pm 0.039	1.646 \pm 0.031
stop1000GeV1	1.092 \pm 0.025	0.264 \pm 0.013	0.046 \pm 0.005
stop1100GeV1000	0.376 \pm 0.011	0.325 \pm 0.01	0.28 \pm 0.009
stop1100GeV100	1.713 \pm 0.023	1.52 \pm 0.021	1.293 \pm 0.02
stop1100GeV10	1.785 \pm 0.023	1.252 \pm 0.019	0.777 \pm 0.015
stop1100GeV1	0.52 \pm 0.012	0.13 \pm 0.006	0.021 \pm 0.003
stop1200GeV1000	0.209 \pm 0.006	0.181 \pm 0.005	0.159 \pm 0.005
stop1200GeV100	0.908 \pm 0.012	0.809 \pm 0.011	0.7 \pm 0.01
stop1200GeV10	0.914 \pm 0.012	0.636 \pm 0.01	0.394 \pm 0.008
stop1200GeV1	0.265 \pm 0.006	0.064 \pm 0.003	0.012 \pm 0.001

Table 17: The signal estimation for $\mu\mu$ isolated in the Signal Regions obtained from MC for Run H.

stop t	SR1	SR2	SR3
stop200GeV1000	3782.613 \pm 159.34	3245.258 \pm 147.242	2712.63 \pm 135.061
stop200GeV100	26095.903 \pm 422.226	22931.305 \pm 396.231	19792.134 \pm 368.385
stop200GeV10	32946.675 \pm 473.292	23726.441 \pm 401.636	15450.694 \pm 323.798
stop200GeV1	9325.404 \pm 250.259	2359.875 \pm 125.969	445.83 \pm 54.423
stop300GeV1000	666.837 \pm 24.525	580.046 \pm 22.878	496.171 \pm 21.132
stop300GeV100	4465.767 \pm 63.018	3899.429 \pm 58.867	3365.214 \pm 54.679
stop300GeV10	5062.744 \pm 67.101	3657.742 \pm 57.009	2371.786 \pm 45.868
stop300GeV1	1569.446 \pm 37.608	421.35 \pm 19.457	88.769 \pm 8.995
stop400GeV1000	172.377 \pm 5.744	148.449 \pm 5.332	127.454 \pm 4.946
stop400GeV100	1056.473 \pm 14.338	935.209 \pm 13.497	803.017 \pm 12.508
stop400GeV10	1184.033 \pm 15.071	857.8 \pm 12.839	565.293 \pm 10.429
stop400GeV1	361.414 \pm 8.343	97.659 \pm 4.346	21.936 \pm 2.069
stop500GeV1000	57.957 \pm 1.772	50.484 \pm 1.657	43.612 \pm 1.541
stop500GeV100	315.529 \pm 4.15	277.165 \pm 3.89	236.849 \pm 3.596
stop500GeV10	349.977 \pm 4.393	251.956 \pm 3.726	163.085 \pm 2.998
stop500GeV1	106.807 \pm 2.401	25.619 \pm 1.175	5.622 \pm 0.553
stop600GeV1000	20.721 \pm 0.617	17.317 \pm 0.565	15.264 \pm 0.53
stop600GeV100	109.765 \pm 1.417	97.31 \pm 1.335	83.71 \pm 1.238
stop600GeV10	118.534 \pm 1.472	84.542 \pm 1.243	54.298 \pm 0.997
stop600GeV1	35.516 \pm 0.804	8.627 \pm 0.397	1.42 \pm 0.163
stop700GeV1000	8.473 \pm 0.244	7.34 \pm 0.227	6.307 \pm 0.211
stop700GeV100	41.224 \pm 0.538	36.613 \pm 0.508	31.299 \pm 0.469
stop700GeV10	44.165 \pm 0.556	31.717 \pm 0.472	20.349 \pm 0.377
stop700GeV1	13.279 \pm 0.306	3.436 \pm 0.156	0.566 \pm 0.064
stop800GeV1000	3.702 \pm 0.105	3.198 \pm 0.098	2.721 \pm 0.09
stop800GeV100	17.906 \pm 0.231	16.008 \pm 0.219	13.782 \pm 0.203
stop800GeV10	18.952 \pm 0.238	13.471 \pm 0.2	8.398 \pm 0.158
stop800GeV1	5.771 \pm 0.131	1.392 \pm 0.064	0.28 \pm 0.029
stop1000GeV1000	0.809 \pm 0.023	0.706 \pm 0.021	0.612 \pm 0.02
stop1000GeV100	3.785 \pm 0.049	3.362 \pm 0.047	2.899 \pm 0.043
stop1000GeV10	3.935 \pm 0.05	2.786 \pm 0.042	1.788 \pm 0.034
stop1000GeV1	1.186 \pm 0.028	0.287 \pm 0.014	0.05 \pm 0.006
stop1100GeV1000	0.408 \pm 0.011	0.353 \pm 0.011	0.304 \pm 0.01
stop1100GeV100	1.861 \pm 0.025	1.652 \pm 0.023	1.404 \pm 0.021
stop1100GeV10	1.939 \pm 0.025	1.36 \pm 0.021	0.844 \pm 0.016
stop1100GeV1	0.565 \pm 0.013	0.141 \pm 0.007	0.023 \pm 0.003
stop1200GeV1000	0.227 \pm 0.006	0.197 \pm 0.006	0.173 \pm 0.005
stop1200GeV100	0.986 \pm 0.013	0.878 \pm 0.012	0.76 \pm 0.011
stop1200GeV10	0.993 \pm 0.013	0.691 \pm 0.011	0.428 \pm 0.008
stop1200GeV1	0.288 \pm 0.007	0.069 \pm 0.003	0.013 \pm 0.001